

Review

Mitigating Environmental Effects in Halide Perovskites through Hybrid Perovskite-Polymer Nanocomposites: A Short Review

Mlungisi Arnold Mavuso ^{1,*}  and Mandla Msimanga ^{1,2} ¹ Department of Physics, Tshwane University of Technology, Pretoria 0083, South Africa² IThemba Laboratory for Accelerator Based Science (LABS), Johannesburg 2050, South Africa; msimangam@tut.ac.za

* Correspondence: mavusoma1@tut.ac.za

Abstract: Metal halide perovskites are currently making notable strides in the development of next-generation optoelectronic and photovoltaic devices. Prototype lab-based devices have exhibited high efficiencies for photovoltaic applications. However, the high performance cannot be maintained for practically useful lengths of time due to degradation of the perovskite layer on exposure to environmental factors such as moisture, oxygen, and heat. This limits the widespread use of these materials in commercial devices. This review of hybrid perovskite-polymer nanocomposites begins by highlighting the significant structural and optoelectrical properties of metal halide perovskites. The discourse moves on to the elucidation of the deleterious effects of environmental stressors on the movement of charge carriers in photovoltaic devices based on these materials. Various mitigatory measures are then considered, with the narrative eventually narrowing down to perovskite-polymer nanocomposites, where the synergistic combination of the two materials is critically analyzed. The conclusion looks at the challenges and opportunities presented by polymer-metal halide perovskite nanocomposites and the potential role they may play in the development of low-cost photovoltaic and optoelectronic devices.

Keywords: metal halide perovskites; photovoltaics; perovskite solar cells; perovskite-polymer nanocomposite



Citation: Mavuso, M.A.; Msimanga, M. Mitigating Environmental Effects in Halide Perovskites through Hybrid Perovskite-Polymer Nanocomposites: A Short Review. *Photonics* **2023**, *10*, 1242. <https://doi.org/10.3390/photonics10111242>

Received: 1 October 2023

Revised: 1 November 2023

Accepted: 6 November 2023

Published: 8 November 2023



Copyright: © 2023 by the authors. Licensee MDPI, Basel, Switzerland. This article is an open access article distributed under the terms and conditions of the Creative Commons Attribution (CC BY) license (<https://creativecommons.org/licenses/by/4.0/>).

1. Introduction

Metal halide perovskites (MHPs) have emerged as excellent semiconductor material candidates for applications in various technologies, including perovskite solar cells (PSCs) [1–3], light-emitting diodes (LEDs) [4–6], and photodetectors (PDs) [7–9]. The widespread interest in these materials is underpinned by several advantages, such as their remarkable optoelectronic properties, low cost, and good solution processability. For instance, MHPs are used as the active layer in PSCs and represent a class of materials with a general structure ABX_3 , where A and B represent the monovalent cations (e.g., methylammonium, CH_3NH_3^+ or MA^+ ; formamidinium, $\text{CH}(\text{NH}_2)_2^+$ or FA^+ ; or cesium, Cs^+) and divalent cations (lead, Pb^{2+} or tin, Sn^{2+}) of different radii, respectively, and X is the halide anion (chloride, Cl^- ; iodide, I^- ; or bromide, Br^-). The coordination of the X^- ions with the B^{2+} ions results in a $[\text{BX}_6]^{4-}$ octahedra occupying each corner of a 3D structural configuration, with the A -site cation filling the voids within the structure, as illustrated in Figure 1a. Between 2009 and 2022, MHPs have shown remarkable strides in the field of photovoltaics, wherein the power conversion efficiencies (PCEs) of solar cells have improved from 3.8% [10] to 26.1% [11], as shown in Figure 1b. Thereby, PSCs have emerged as potential alternatives to crystalline silicon (Si)-based single-junction solar cells (SCs), which currently monopolize the photovoltaic (PV) industry with approximately 90% of the market share.

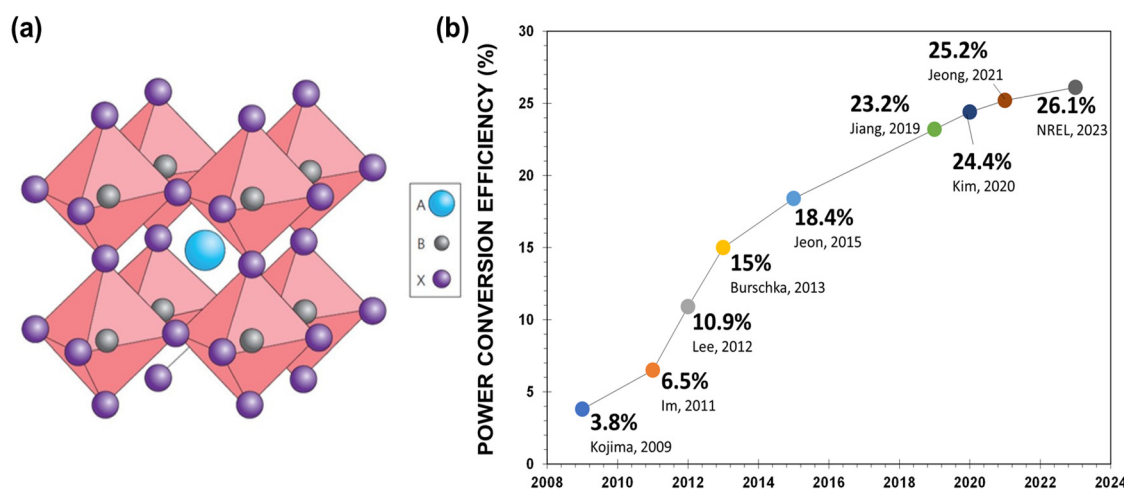


Figure 1. (a) The general crystalline structure of ABX_3 metal halide perovskites [12]. (b) Evolution of the PCEs of PSCs [10,11,13–19].

The structural and chemical configuration of some MHPs leads to impressive optoelectronic properties such as direct tunable band gap energies, long charge-carrier lifetimes, a large absorption coefficient, high ambipolar charge mobility, long carrier diffusion lengths, small exciton binding energy, and high defect tolerance [20–23]. Recent developments in nanostructured MHPs such as quantum dots (QDs) [24], nanosheets (NSs) [25], and nanowires (NWs) [26,27] demonstrate that these structures exhibit strong quantum confinement effects and improved optoelectronic properties compared to their bulk counterparts. The development of perovskite opto- and nanoelectronic materials and devices enjoy much attention in contemporary research in the field. Moreover, the rapid improvement in their photo conversion efficiency has increased the call for the commercialization of MHP-based PV devices.

Despite all these significant achievements in the development path of MHPs with excellent properties, these materials still exhibit negative material attributes that limit their widespread application in practical devices. Long-term stability issues caused by the irreversible structural decomposition of the MHPs due to moisture, oxygen, and ultraviolet (UV) radiation, low thermal stability, and lead toxicity have been major stumbling blocks that limit their use, as summarized in Figure 2. The resultant functional limitations due to these problems are elucidated further in Section 2.3. In the quest to overcome these drawbacks and structural inadequacies associated with MHPs, several techniques have been (and are being) developed to prepare highly stable MHP films with improved optoelectrical performance. One approach, among others, has been to introduce suitable polymers into the MHP matrix (or, conversely, embed MHP nanoparticles in a polymer matrix) to form hybrid nanocomposites that combine the properties of either material in a synergistic way.

In this review, a detailed summary of recent developments in perovskite-polymer nanocomposites aimed at improving the stability and performance of PSCs, LEDs, and PDs is presented. The review starts with a discussion of the chemical nature and properties of pure MHPs of different stoichiometric configurations, followed by their environment-induced functional inadequacies, which point to the need for alternative structures such as hybrid perovskite-polymer nanocomposites. Fabrication techniques such as physical and chemical anchoring of polymers onto the MHPs to form perovskite-polymer nanocomposites are next discussed. Several synergistic effects in perovskite-polymer systems are then elucidated by examining the role of polymers in the improvement of the long-term stability and performance of PSCs, LEDs, and PDs, with an emphasis on charge transport characteristics.

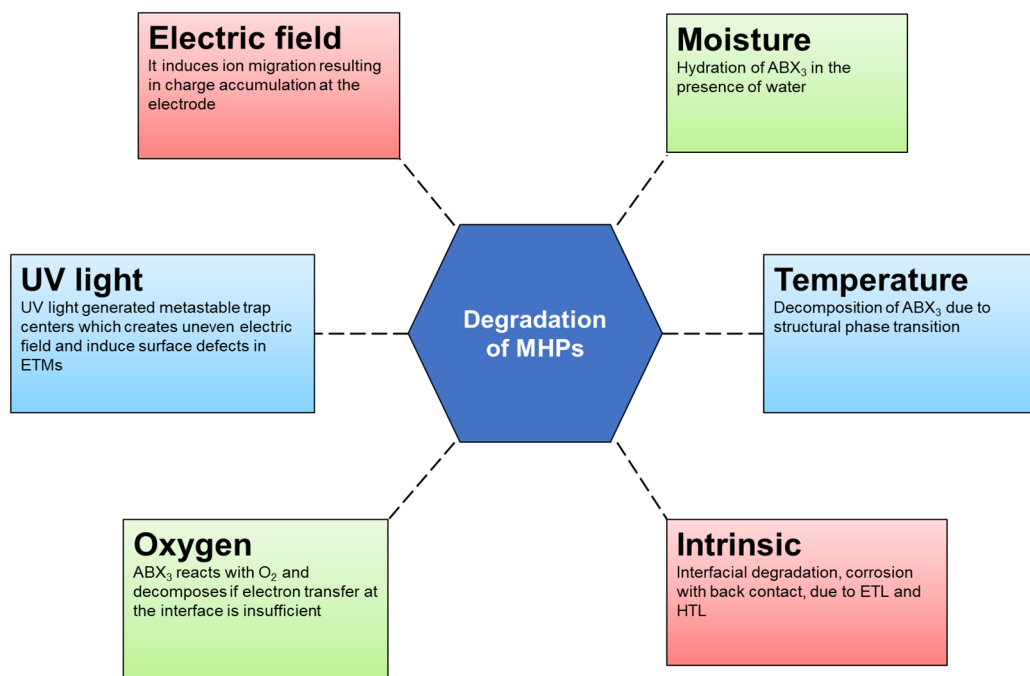


Figure 2. Schematic representation of several factors causing degradation of MHPs [28].

2. Structure, Properties, and Ambient Degradation of Perovskites

2.1. Crystal Structure

Hybrid MHPs generally have either a cubic, tetragonal, or orthorhombic crystal structure, as illustrated in Figure 3. For instance, MAPbI_3 is known to exhibit the tetragonal phase ($a = b \neq c$) at room temperature. At lower temperatures, the tetragonal symmetry is broken down and the orthorhombic structure is observed ($a \neq b \neq c$). At temperatures higher than room temperature, the symmetry of the structure increases, and the cubic crystal structure ($a = b = c$) may result [29]. In the general ABX_3 chemical formula typical of perovskites, the A-site cation is a larger cation compared to the B-site cation. The A-site cation occupies the cubo-octahedral site surrounded by twelve anions, while the B-site cation occupies the octahedral site shared with six anions [30–32].

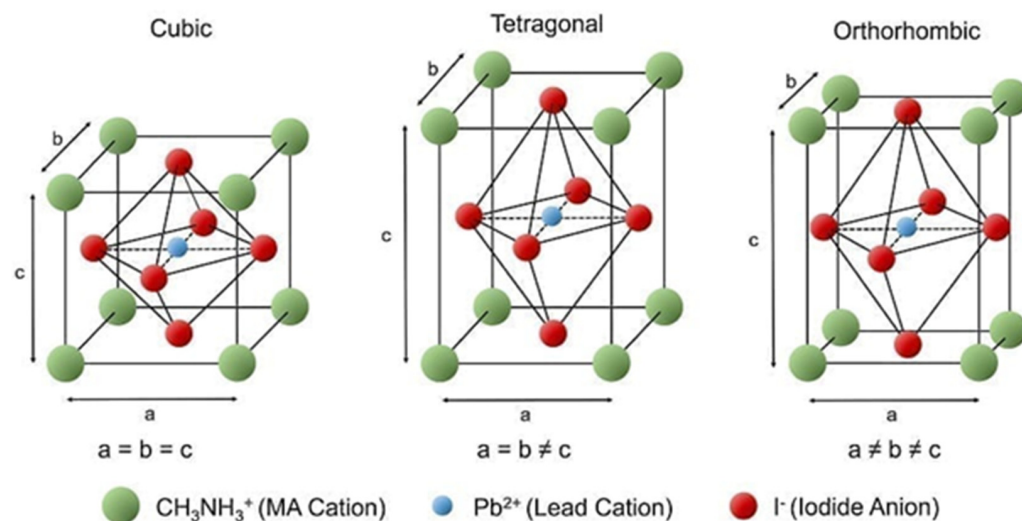


Figure 3. Three types of perovskite unit-cell phases of a typical organometal halide perovskite [29].

It is widely acknowledged that 3D nanostructures present a larger surface area for photon-matter interactions when compared to lower-dimensional structures. In the design

of new perovskite architectures for optoelectronic applications, there is a heightened focus on 3D versions of different perovskite materials [33]. The dimensions of the perovskite structure depend on the radial size of the *A*-site and *B*-site cations and *X*-site anions. A 3D perovskite structure can be obtained when the different atomic and molecular species in the unit structure satisfy the Goldschmidt tolerance factor (*t*) [34], defined as:

$$t = (r_A + r_X)/[\sqrt{2} (r_B + r_X)] \quad (1)$$

in which r_A , r_B , and r_X refer to the ionic radius (*r*) of *A*, *B*, and *X*, respectively [34]. Generally, most MHP materials preserve the 3D architecture and are formed in the range of $0.81 \leq t \leq 1.1$. Specifically, ideal cubic structures are found within $0.9 \leq t \leq 1.0$, and orthorhombic or rhombohedral structures can be found in the range $0.71 \leq t \leq 0.9$ [30–37]. When $t \leq 0.71$ or $t \geq 1$, other crystal structures, such as hexagonal and A_4BX_6 -type structures, may be formed. When $t < 0.7$, the *A*-site monovalent cation is too small to form the perovskite due to distortion of the structure. If $t > 1$, the *A*-site cation is too large, leading to alternative structures [38,39]. The octahedral factor, defined as $\mu = r_B/r_X$, can be employed to assess the suitability of the *B*-site divalent cation to form into the $[BX_6]^{4-}$ octahedron. This factor should vary between 0.44 and 0.90 in order to form a stable cubic perovskite structure [36–40]. Therefore, the combination of Goldschmidt's tolerance factor and octahedral factor allows for the screening of probable 3D perovskite structures from a plethora of possibilities. Figure 4 shows the tolerance factors vs. octahedral factors graph for 12 of the most common MHPs [40].

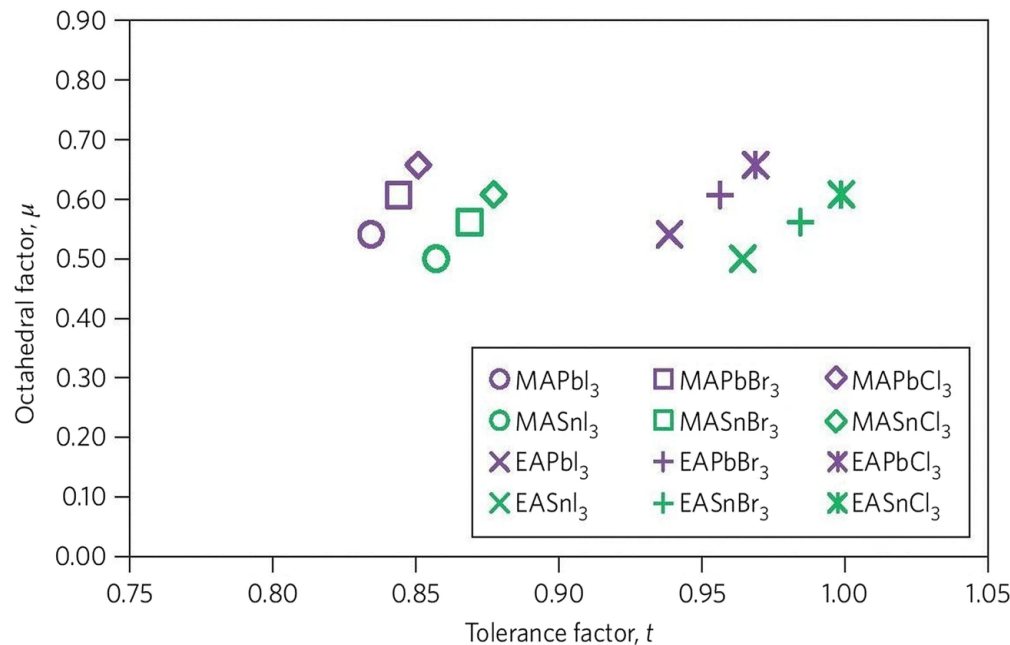


Figure 4. The estimated *t* and μ factors for 12 common metal halide perovskites [40].

2.2. Optical and Electrical Properties

Hybrid MHPs have exhibited excellent optical properties that have proven pivotal in numerous light-related applications, including PDs, LEDs, and PV cells. They have notable intrinsic properties such as: (1) high photon absorption coefficient (10^4 – 10^5 cm^{−1}); (2) tunable band gap (1.28–1.55 eV); (3) large diffusion length for charge carriers (100 nm–100 μ m); (4) ambipolar carrier transport ability; and (5) high charge carrier mobility (100–1000 cm²V^{−1}s^{−1}) [41]. These classes of perovskite also exhibit high photoluminescence yield and lifetime. All these properties depend, in one way or another, on the crystal structure and chemical composition of the material. For instance, Hong Noh and colleagues [42] successfully demonstrated that lattice parameters and band gap energy

have a linear relationship with the halide content in $\text{MAPb}(\text{I}_{1-x}\text{Br}_x)_3$, as shown in Figure 5. Through band gap engineering, the optical absorption of MHPs can be tuned to specific optoelectronic and PV applications [42,43]. The band gap can also be modulated by adjusting the morphology of the MHPs. The Lai et al. [27] study demonstrated that MHP NWs exhibited a lowering of the band gap from 2.78 to 1.76 eV with a higher photoluminescence compared to their planar configuration [27]. According to density functional theory (DFT) analysis, the perovskite band structure near the band edge is governed by the $[\text{BX}_6]^{4-}$ octahedra [44,45]. Substituting the *B*-site cation and *X*-site anion can shift the band energy levels, which leads to a change in the bandgap energy. The valence band (VB) maximum contains antibonding states derived from the hybridization of the *B* metal *s*-orbitals and the halide *p*-orbitals, while the conduction band (CB) minimum is made up of the interaction between the *B* metal *s*-orbitals and *X* *s*-orbitals. Therefore, the *B*–*X* bond length is considered important in determining the optical band gap of MHPs [44,46–50]. It is found that defect states within MHPs are formed in the CB and VB band energy levels, but the bandgap of MHPs is defect- or trap-site-free. Interstitial and anti-site defects are uncommon in MHPs and do not affect the radiative recombination processes, thus making MHPs highly defect-tolerant materials [50].

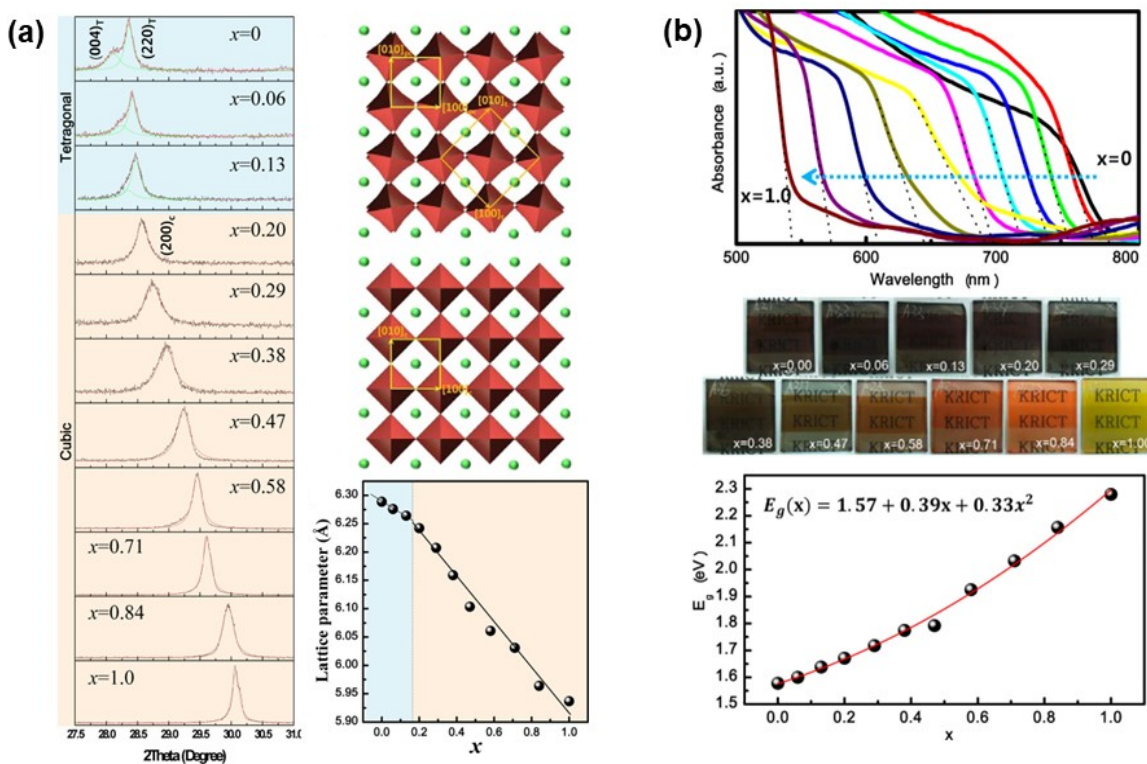


Figure 5. (a) Crystal lattice parameters and (b) band gap energy as a function of the halide (X) content in the mixed halide MHPs [42].

MHPs have excellent electrical properties that have proven invaluable for electrochromic, photo-sensing, and PV applications. The charge carrier mobility is found to be relatively high in these compounds. For instance, the electron mobility is estimated to be $\sim 66 \text{ cm}^2 \text{ V}^{-1} \text{ s}^{-1}$ for MAPbI_3 , $\sim 103 \text{ cm}^2 \text{ V}^{-1} \text{ s}^{-1}$ for FASnI_3 , $\sim 270 \text{ cm}^2 \text{ V}^{-1} \text{ s}^{-1}$ for $\text{MASn}_{0.5}\text{Pb}_{0.5}\text{I}_3$, $\sim 536 \text{ cm}^2 \text{ V}^{-1} \text{ s}^{-1}$ for CsSnI_3 , and $\sim 2320 \text{ cm}^2 \text{ V}^{-1} \text{ s}^{-1}$ for MAPbSnI_3 , while the hole mobility is estimated to be $\sim 322 \text{ cm}^2 \text{ V}^{-1} \text{ s}^{-1}$ for MASnI_3 and $\sim 520 \text{ cm}^2 \text{ V}^{-1} \text{ s}^{-1}$ for CsSnI_3 [51,52]. The charge carrier mobility of MHPs is dependent on the different morphologies of the MHP crystals [27,53]. Various large crystals of MAPbX_3 have exhibited higher charge carrier mobilities than the original estimates of $25 \text{ cm}^2 \text{ V}^{-1} \text{ s}^{-1}$ and $66 \text{ cm}^2 \text{ V}^{-1} \text{ s}^{-1}$ for thin films and pressed pellets, respectively [53]. MAPbX_3 crystals grown from hydrohalic acids

have shown a mobility of $\sim 164 \text{ cm}^2 \text{V}^{-1} \text{s}^{-1}$ and a charge diffusion length of $175 \mu\text{m}$ [54]. This value far exceeds the diffusion length obtained in thin films prepared under the “ $\text{MAPbI}_{3-x}\text{Cl}_x$ ” protocol ($\sim 1 \mu\text{m}$). Single-crystalline MAPbX_3 grown from hydroiodic acid (HI) has exhibited a record mobility of $\sim 800 \text{ cm}^2 \text{V}^{-1} \text{s}^{-1}$ within the first few femtoseconds of photoexcitation [55]. According to Stoumpos et al., (2016) [53], Sn-containing MHPs have exhibited high electron mobilities, with the highest reported values of $\sim 585 \text{ cm}^2 \text{V}^{-1} \text{s}^{-1}$ and $\sim 150 \text{ cm}^2 \text{V}^{-1} \text{s}^{-1}$ for CsSnI_3 and MASnI_3 , respectively [52,53]. Similar to the optical properties, the charge transport properties are linked to the composition and thickness of the MHP thin films. Zhang et al. (2014) [56] demonstrated that the charge transport properties of all-inorganic CsSnI_3 perovskite thin films increased proportionally with film thickness. The study showed that the hole mobilities at room temperature increased from ~ 3 to $20 \text{ cm}^2 \text{V}^{-1} \text{s}^{-1}$ as film thickness increased from 150 to 600 nm [56]. Additionally, migration of the halide ion within the MHP led to unusual electrical behavior caused by the presence of native point defects or lattice distortion [57–59]. This unusual electrical behavior could be attributed to the photocurrent hysteresis, which impacts the stability of the MHP solar cells. Hoke and co-workers (2014) [60] illustrated the occurrence of serious phase segregation in mixed halide $\text{MAPbBr}_{x}\text{I}_{3-x}$ films under illumination. The study showed a splitting of X-ray diffraction (XRD) peaks, which is consistent with photo-induced halide segregation. The red shift in the photoluminescence spectrum (PL) upon illumination resulted in a reduced electronic band gap and split quasi-Fermi level, leading to a lowered open-circuit voltage in solar cells [57,61]. This photo-induced instability is expected to impact the operation and reliability of other optoelectronic devices made from MHP materials [56].

2.3. Deleterious Effects of Environmental Factors

Despite the numerous advantages associated with MHPs, there are several drawbacks hindering widespread commercial applications of MHP-based devices. Current research efforts in PSCs are largely focused on enhancing their long-term environmental stability due to the vulnerability of the active perovskite layer to environmental factors such as moisture, heat, air/oxygen, and UV light [28,32,61]. Effective device design strategies to work around functional inadequacies due to these environmental stressors require thorough elucidation of the degradation mechanisms and structural defects that they cause. The following sub-sections highlight some of the main problems caused by environmental factors in metal halide perovskites.

2.3.1. Moisture

Moisture is one of the key factors that accelerates the decomposition of MHPs. Typically, organic cations MA^+ and FA^+ are hygroscopic and hydrolyze in the presence of moisture [61,62]. The acidic nature of MA leads to the formation of H_3O^+ ions by breaking the bond between the A-site and B-site components of the MHPs [28,61]. Studies suggest that exposure to moisture leads to the formation of a hydrohalic acid (HX ; $\text{X} = \text{I}, \text{Cl}$, or Br), which is soluble in water [28,31,32,41,59,61–63]. Although small amounts of water are required to deprotonate the organic A-site (MA^+), excess water will be required to completely dissolve HX and MA byproducts for the degradation reaction to continue. The degradation process that occurs due to the presence of water is a series of self-sustaining closed-loop reactions. Trace amounts of water will result in partial decomposition of the MHP, and byproducts will reach equilibrium. Excess amounts of water will completely degrade the MHP to form metal halide (MX_2) [41,63]. The following reactions denote the possible degradation mechanism in the presence of water [63]:





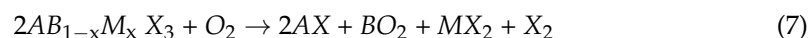
where A , B , and X represent the inorganic or organic A -site monovalent cation (FA^+ , MA^+ , and Cs^+), metal B -site divalent cation (Pb^{2+} and Sn^{2+}), and halide monovalent anion (Br^- , Cl^- , and I^-), respectively. When a MHP is exposed to moisture, it will lead to the decomposition of ABX_3 into AX and BX_2 (as shown in Equation (2)). In an aqueous solution, the AX can further decompose to form the A and HX solutions (see Equation (3)) [41]. The acidic HX can further compose in two ways: (a) by reacting with the atmospheric O_2 to form X_2 and H_2O , which make the reaction self-sustaining; and (b) by decomposing with UV light irradiation to form X_2 and H_2 gas [41].

2.3.2. Oxygen

Most MHPs have demonstrated good resistance to oxygen when left in the dark, clearly indicating the relative stability of most MHPs in their ground state. However, the MHPs can quickly decompose in the presence of both oxygen and light. For instance, Pearson et al. [64] report that $MAPbI_3$ -containing devices exhibited a 20% absorber degradation within the first few hours of sun exposure in the presence of oxygen. It is believed that the photodecomposition reaction mechanism in the presence of oxygen is dictated by defects such as iodide vacancies [61,65]. The diffusion of molecular oxygen into the bulk of $MAPbI_3$ films happens immediately upon exposure and is complete within an hour. The oxygen is usually absorbed and diffused through iodide vacancies at both the surface and bulk of the $MAPbI_3$ crystallites. The iodide vacancy densities have been predicted to be inherently high and can be generated quickly when photo-activated [61]. These vacancy sites occupy a similar volume to oxygen, which allows for an easy pathway for oxygen into the MHP lattice. At the vacancy site, molecular oxygen acts as an electron trap site in the conduction band of an MHP. The trapped electrons are responsible for the formation of highly reactive superoxide anions ($\bullet O_2^-$), which initiate an acid-base reaction with the acidic A -site cation in MHPs. Furthermore, $\bullet O_2^-$ reacts with the A -site cation in MHPs to give H_2O , a deprotonated A -site gas, and BX_2 as a product [61,66]. Sn-based MHPs are less stable to oxygen than lead-based MHPs and can oxidize in the dark due to the susceptibility of $Sn(II)$ to easily oxidize to the $Sn(IV)$ state. For instance, $MASnI_3$ PSCs have demonstrated rapid degradation when exposed to air for even several seconds [67]. The typical oxidation mechanism of MHPs is:



The formation of BX_4 is the driving factor in the oxidation of Sn-based MHPs. The reaction proceeds by minimizing the amount of broken $B-X$ bonds, thus allowing for a low-energy pathway to oxidation of the MHP layer in PSCs. The oxidation pathway can only occur if there are multiple adjacent $[BX_6]^{4-}$ octahedra accessible to the migration of iodine from one metal atom to another to form BO_2 and BX_4 . However, this oxidation pathway can be slowed down by reducing the formation of BX_4 due to the fewer available $[BX_6]^{4-}$ octahedra. A common technique used to reduce the formation of BX_4 involves introducing a second metal into the B -sites of MHPs. This reaction pathway will form X_2 alongside BO_2 and MX_2 :



This reaction pathway requires breaking twice as many $B-X$ bonds, leading to higher activation energies. A strategy that involves mixed B -site compositions could result in enhanced material stability.

2.3.3. UV Light

Though many studies have previously reported that in the absence of both oxygen and moisture, most MHPs can maintain their photocurrent for hundreds of hours upon light exposure, there is evidence of significant changes in MHPs during light exposure, including halide segregation, ion migration, and compositional degradation [32,61]. In addition to the MHP absorber layer, the charge transport layers used in PSCs are also susceptible to photo-induced instability. Titanium dioxide (TiO_2) electron transport layers (ETLs), for instance, have exhibited extreme instability towards UV light even in inert operational conditions [32,61,67]. Leijtens et al. [67] describe the rapid decay in open circuit voltage and photocurrent of TiO_2 -containing PSC devices within hours of UV light exposure in inert environments [67]. According to the degradation pathway, the induced rapid recombination usually occurs across the MHP–HTL or TiO_2 –MHP interface, where the changes in the charge transport layer result in drastic losses in device performance. Upon UV light exposure, the photo-generated holes react with the absorbed oxygen on surface oxygen vacancies, thereby acting as deep trap sites that lead to charge recombination [67].

2.3.4. Heat

Most MHP crystal structures are highly sensitive to heat due to a series of successive phase transitions in the MHP crystal structure as the temperature increases. At low temperatures ($T < -110.9^\circ\text{C}$), MHPs exhibit a distorted orthorhombic crystal structure [68]. As the temperature increases, they show a tetragonal phase at mid-range temperatures ($T = -110.9$ to 54.4°C) and then an ideal cubic phase at higher temperatures ($T > 54.4^\circ\text{C}$) [69]. However, further increases in temperature causes structural decomposition that produces volatile *A*-site and *HX* compounds. The thermal stability of MHPs has serious implications for the sustainability of continuous exposure to sunlight, which could affect the crystal structure and phase of the MHPs. Therefore, the annealing temperature (60 – 150°C) and time (10 min to 2 h) have become important in attaining the desired phase for the long-term stability of MHPs [41,69]. The hole transport layers (HTLs) in MHPs-containing PV devices are also susceptible to thermal instability since the majority of these HTL materials are organic materials such as poly(3,4-ethylenedioxythiophene) (PEDOT) and 2,2',7,7'-Tetrakis[N,N-di(4-methoxyphenyl)amino]-9,9'-spirobifluorene (Spiro-OMeTAD). Thermal instability of these materials becomes more pronounced when a multi-functional additive such as 4-*tert*-butylpyridine (tBP) and lithium bis-trifluoromethanesulfonimide (Li-TFSI) is used to improve the conductivity [70–73]. Spiro-OMeTAD has been reported to degrade at high temperatures via multiple mechanisms. The additive tBP used in Spiro-OMeTAD and poly(triaryl amine) (PTAA) HTL materials can evaporate at temperatures as low as 85°C , and Spiro-OMeTAD can crystallize within a few hours at 100°C , thereby degrading the PV cell efficiency [73]. Researchers have reported the formation of voids in devices using Spiro-OMeTAD with tBP and Li-TFSI additives at 80°C for one hour, even in devices without an MHP layer [73].

2.4. Perovskite-Polymer Nanocomposites for Improved Stability

Recently, polymer/MHP nanocomposites have been proposed by research groups for application in several PV devices, including flexible PV cells, LEDs, and PDs. Polymer/MHP nanocomposites have shown favorable properties that can help mitigate the drawbacks found in MHP-containing devices that lead to energy loss in the cell. Since the main energy losses within MHP-based devices can be attributed to non-radiative recombination, affecting the charge transport processes, the dominant sources responsible for the non-radiative recombination losses in PSCs are defect capture and mismatched energetic alignment at the interfaces [41]. Therefore, efficient control of the trap density and modification of the interfacial properties will prove pivotal in alleviating the undesirable effects originating from the interfacial recombination losses [74]. The trap site-induced non-radiative losses could lead to an accumulation of charge carriers and impair the optoelectronic properties of PSCs, LEDs, and PDs [61,74–77]. In terms of long-term device

stability, the non-radiative recombination centers potentially serve as the ion migration pathways and adsorption sites for water and oxygen in air, thereby accelerating the degradation of the MHP layers and metal contact corrosion [61]. Moreover, the defect sites can trap the charge carriers and may promote the deprotonation of the organic A-site cation by the electrical field [28]. The instability of the molecular components in MHP films further hinders device durability and environmental resistance. To improve the practical use of MHPs, some degree of protection against decomposition in the ambient environment is required.

Over the last few years, the development of protective strategies has shown promising results in improving the long-term stability of MHP devices. These strategies include: (1) protective coatings; (2) cross-linking of ligands; and (3) polymer blends [78]. Polymeric materials possess several advantages for both interfacial passivation and environmental tolerance due to their low cost, low toxicity, high transparency, high polarity, and facile film fabrication [71,78,79]. Reported work on polymeric passivation layers shows that introducing a thin layer of polymer at the MHP–ETL interface greatly reduces the work function of the metal oxide ETL due to the formation of an interfacial dipole without affecting the morphology, transparency, or hydrophilicity of the ETL [77], thereby reducing the degradation at the MHP–ETL interface. Further, since most MHPs are known to be highly susceptible to environmental stressors, particularly water from the environment, which leads to the degradation of the MHP layer to form metal halide and organic salts, polymeric materials can offer steric resistance against external stressors due to their strong hydrophobicity and low volatility [80].

It is worth noting that polymeric additives can be an effective method to mitigate the above-mentioned drawbacks of MHPs. Some polymeric materials, such as polystyrene (PS) [78], poly(methyl methacrylate) (PMMA) [74,78,80], poly(vinylpyrrolidone) (PVP) [81–83], polyvinylidene fluoride (PVDF) [84], and polyaniline (PANI) [85,86], have been used as protective polymer films in PSCs. These polymers have been used to not only passivate the surface defects but also block atmospheric moisture, which improves the stability of PSCs even in high-humidity environments. Figure 6 denotes the typical perovskite-polymer nanocomposites for the design of PV cells.

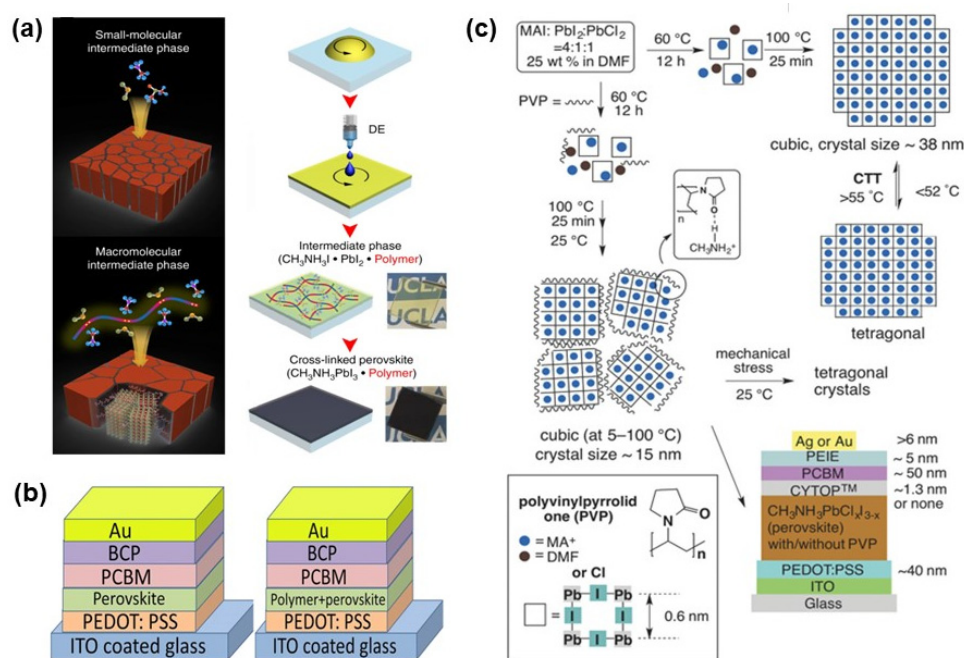


Figure 6. Perovskite/polymer nanocomposite-based PV cells: (a) polymer-perovskite composite cross-linker [87]; (b) schematic architecture diagram of the PV devices fabricated from MAPbI₃ and PTB7-MAPbI₃ composite, respectively [88]; (c) PVP-modified MAPbI_{3-x}Cl_x nanocrystals for semitransparent solar cells [89].

3. Fabrication of Polymer-Perovskite Nanocomposites

Polymer/MHP nanocomposites exhibit simultaneous size and morphology control, enhanced stability, and suppressed solid-state agglomeration [78,84,90,91]. In addition to improved environmental stability, PV devices prepared using polymer/MHP nanocomposites possess processing flexibility, stretchability, and self-healing properties inherited from the polymers [81,92,93]. There are many strategies that have been proposed and adopted by researchers for the preparation of polymer/MHP nanocomposites for PV applications, including LEDs, PDs, PSCs, and lasers. Some of these fabrication techniques are discussed in the section below.

3.1. Blending Polymers with MHP Nanocrystals

Physical blending of MHP nanocrystals (NCs) with a plethora of polymer solutions, such as PMMA, PS, poly(styrene-ethylene-butylene-styrene) (SEBS), and poly(lauryl methacrylate) (PLMA), has been explored to form nanocomposite materials with enhanced stability and processability for PV devices [92,94]. Many MHP-polymer nanocomposites are prepared through modified spin-coating approaches to produce films with uniform size, thickness, and morphology [74,85,94,95]. Physical blending has been viewed as a simple, effective, and scalable technique for the large-scale commercialization of MHP-polymer nanocomposites. For example, Kafetzi et al. [94] demonstrated physically blended MAPbBr_3 /poly(methyl methacrylate-co-(dimethylamino) ethyl methacrylate) or P(MMA-co-DMAEMA) hybrid nanocomposite with improved optoelectronic properties. The copolymer was prepared separately via conventional free radical polymerization and dissolved in toluene. The MAPbBr_3 colloids were prepared by dissolving in *N,N*-dimethylformamide (DMF), and then the colloids were added to the copolymer solution to form the MHP-polymer colloidal system, as shown in Figure 7. The study found that the self-organization of P(MMA-co-DMAEMA) random copolymer in toluene results in the formation of nanoaggregates, where the DMAEMA parts make up the nanoparticle core and the MMA units are the corona. Adding MHP-DMF solution to the colloid copolymer solution results in the encapsulation of the MHP nanocrystals into the DMAEMA matrix, while the MMA functions as a colloid stabilizer. The MAPbBr_3 /P(MMA-co-DMAEMA) solution exhibited improved stability lasting for more than a month in some instances [94].

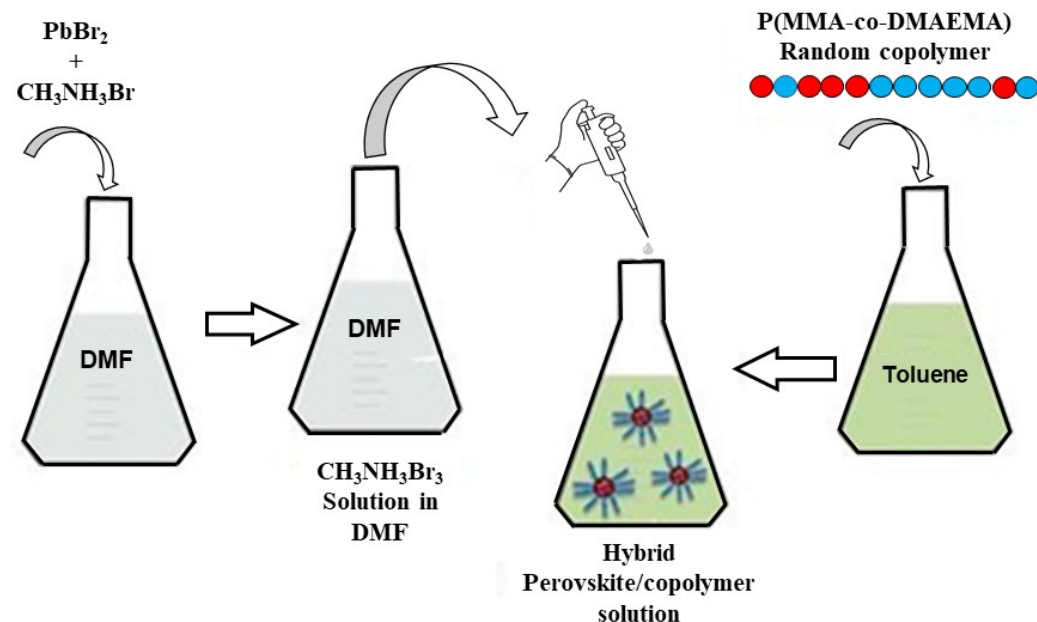


Figure 7. Preparation of perovskite/polymer nanocomposites by physical blending [94].

Another physical blending strategy for the fabrication of MHP/polymer nanocomposites is the “swelling-shrinking” technique [92,93]. Polymer chains will swell and expand

when they encounter good solvents, thereby letting the solvents and solutes into the polymeric matrix [92]. Generally, the expansion is often reversible through the deswelling or shrinking process when the solvent is evaporated. The swelling-shrinking technique involves exploiting the differences in the solubility of polymers in certain solvents. The technique can achieve well-dispersed, passivated MHP NCs embedded in the polymer matrices. As a result, the MHP/polymer nanocomposite films possess high photoluminescence efficiency, color purity, and enhanced stability against heat and water exposure [94].

Electrospinning is another physical blending technique that is widely used to fabricate one-dimensional fibrous nanomaterials. Electrospinning can be used to convert nanofibers into light-emitting devices for flexible or wearable electronic products. This technique can be used to prepare fibrous MHP/polymer nanocomposites for PV applications due to their light weight, flexibility, controllable properties, and low cost [81,82,95].

3.2. In-Situ Formation of Perovskite in Polymers

Premade MHP nanocrystals can be exposed to solvents and environments during processing, leading to progressive deterioration of the crystal structure prior to incorporation into the polymer matrix. Sometimes, the surface ligands on MHPs and the polymer matrix can be incompatible, which may inhibit high-quality and uniform nanocomposite film formation without phase separation. Therefore, it is sometimes advisable to synthesize the MHP nanocrystals within the polymer matrix by controlling solvent evaporation. Typically, MHP-polymer nanocomposites are prepared by dissolving a mixture of perovskite precursor and polymer in a suitable solvent and then drop-casting or spin-coating onto a glass or plastic substrate. The coated substrate then undergoes a two-stage controlled solvent evaporation process [92]. In the first stage, the solvent is rapidly and partially removed by vacuum drying, leading to polymer crystallization and the formation of multi-colored or transparent thin films. The residual solvent within the polymer matrix has been found to inhibit the simultaneous crystallization of MHP nanocrystals, leading to a uniform distribution of the MHP precursors [92]. The second stage then involves the slow drying of the residual solvent in ambient conditions, which gradually leads to the encapsulation of the MHP nanocrystals in the polymer matrix. In Masi and co-workers' study [90], in-situ synthesized MHP/polymer nanocomposites exhibited films with uniform size and distribution of MHP nanocrystals in the polymer matrix, due to a strong interaction between A-site cations in the precursor and functional groups of the polymer. Particularly, the hydrogen bonds were found to be responsible for the interaction between the A-site cation and the polymer. Furthermore, the basic nature of the ester moieties, steric hinderance, and hydrogen binds of donor or acceptor groups in polymers govern this polymer interaction with the A-site cation. Further, the MHP/polymer nanocomposites exhibited improved moisture stability when compared to pristine MHPs [90].

Hu and co-workers [96] successfully prepared MAPbBr₃/poly(2-methoxyethylacrylate-co-N-isopropylacrylamide) nanocomposites with luminescence and self-healing properties using an in-situ synthesis engineering technique. As shown in Figure 8a, the copolymer was prepared by a modified bulk copolymerization method, where the co-monomers were mixed in a glass bottle while stirring in ice water. The copolymerization process was initialized by tetramethyl ethylenediamine (TEMED) and potassium disulfate (K₂S₂O₈) and allowed to proceed for a further 24 h at 25 °C. Thereafter, the copolymer was dispersed into a mixture precursor solution comprising MABr₂, PbBr₂, oleic acid (OA), and oleyl amine (OAm) in the solvent *N,N*-dimethylformamide (DMF). The resultant solution was cast or spin-coated onto a glass substrate and dried in a vacuum oven at 25 °C. Data from XRD, HRTEM, FTIR, and XAFS demonstrated that the copolymers act as a unique matrix to control the growth process of MAPbBr₃ nanocrystals, resulting in smaller MAPbBr₃. Furthermore, the luminescence and self-healing properties of the nanocomposites were attributed to the surface interaction between MAPbBr₃ nanocrystals and the functional groups of the copolymer [96]. The study proposed that the copolymer chain could anchor on the MAPbBr₃ NCs surface through a coordination bond between its carboxyl group

and the Pb^{2+} of MAPbBr_3 NCs, as well as the hydrogen bond between the protonated acylamino in the polymer and the Br^- of MAPbBr_3 NCs, which improves the crosslinking density in the nanocomposites [96].

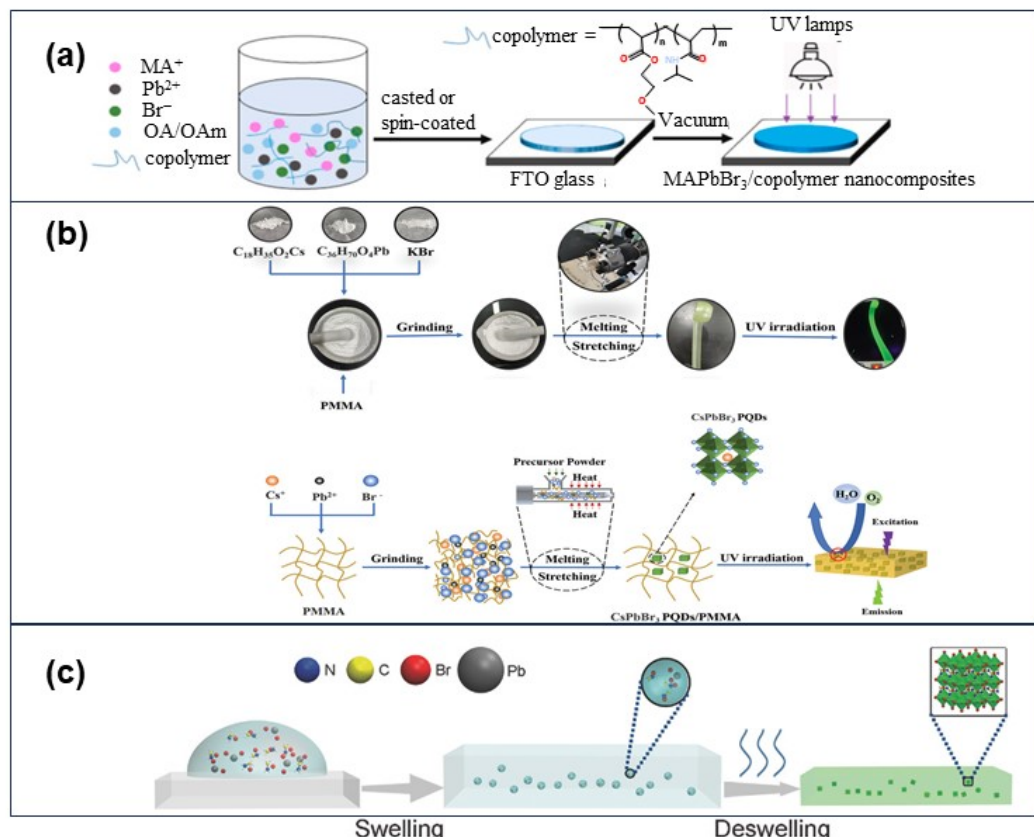


Figure 8. In-situ preparation of perovskite/polymer nanocomposites by (a) solution processing [96]; (b) polymer melt encapsulation [80]; and (c) “swelling-shrinking” encapsulation technique [97].

A study by Wang et al. [80] also demonstrated that CsPbBr_3 -PQDs/PMMA nanocomposites could be prepared via the in-situ polymeric melt encapsulation method, as shown in Figure 8b. The PQDs/polymer nanocomposites were prepared by mixing Cs-, Pb-, and Br-containing precursors into a pastel and mortar. The PMMA was added to the solid-state solution, and the solid mixture was ground into a fine powder. The precursor powder was then melted at 180–220 °C for 30 min and rotated at 200–800 rpm under ambient conditions. Afterward, the melt was cooled and injected into plates using a flat nozzle. The prepared CsPbBr_3 -PQDs/PMMA nanocomposite showed excellent photoluminescence performance of ~82.7% PLQY with a ~18.6 nm full width at half-maximum (FWHM) of PL peak, and the charge carrier decay was calculated to be 32.5 ns, indicating an improved charge lifetime compared to pristine PQDs. After 90 h of UV irradiation or 35 days of heating at 60 °C, the luminous intensity remained almost unchanged. Additionally, after soaking in water for 15 days, the composite retained up to ~53% of the initial luminous intensity, demonstrating long-term stability against UV irradiation, heat, and water [80].

Other techniques that combine “swelling-shrinking” encapsulation and electrospinning techniques can be utilized for the in-situ synthesis of MHP nanocrystals within a polymer matrix, as shown in Figure 8c. By blending the perovskite precursors instead of the MHP itself, MHP crystal decomposition can be prevented. Typically, perovskite precursors and selected polymers are mixed in a solvent to form a homogeneous solution. Following that, the solution is dropped onto specific substrates to give thin-film nanocomposites without the addition of poor solvents such as toluene and hexane. The evaporation of the solvent induces the fast crystallization of MHP and nanocrystals within the shrunken polymer matrices [97]. The electrospinning method can be used through the incorporation

of perovskite precursors in polymers to form fibrous MHP-polymer nanocomposites. Usually, the perovskite precursors are simultaneously and coaxially electrospun in solvents, which facilitates the *in-situ* crystallization of MHP nanocrystals within the polymer after evaporating the solvents [93]. The morphological and photophysical properties of the MHP nanocrystals inside the fibers are effectively modified by controlling the composition and stoichiometry of perovskite precursors, polymer loading, solvent composition, and concentrations.

3.3. Simultaneous Synthesis of Perovskite and Polymer Polymerization

The agglomeration of MHP nanocrystals is usually caused by the high surface-to-volume ratio, which results in high surface energies. Therefore, polymers have been widely used in the colloidal fabrication of MHP/polymer nanocomposites to stabilize the MHPs' surface. Chemically anchoring polymers onto MHP nanocrystals can eliminate phase separation between polymers and the MHPs due to their strong chemical interactions, which gives a different product from physical blending [78,90]. This can be achieved through *in-situ* synthesis of the MHPs in a pure monomer solution, followed by polymerization of the monomer via thermal- or UV-light-induced photopolymerization [78]. This chemical anchoring of the polymer onto the MHPs has been seen to lead to improvements in the structural integrity and stability of MHP/polymer nanocomposites when compared to pure MHPs. Moreover, these nanocomposites have been found to be highly soluble in organic solvents, which makes them relatively highly solution-processable.

4. Charge Transport Properties of Polymer-Perovskite Nanocomposites

The preceding section cites a few examples of the improved stability of perovskite-polymer nanocomposites against environmental stressors such as moisture and oxygen. The polymer matrix serves to passivate surface defects that act as charge trap centers that degrade device efficiency in PSCs. Wang et al. reported that amine-functionalized cyclohexene molecules favor charge carrier transport and surface or interfacial passivation [98]. These molecules combine a hydrophobic benzene ring and a π conjugate structure with an amino group that can implant the molecule into the $B-X$ structure through coordination with the B -site ions or hydrogen bonds [76,99]. Particularly, conjugated polymers can assist in band energy level alignment, which allows effective charge separation at the MHP/polymer interface and increases charge carrier lifetime. The π -conjugated system, which involves double and single bonds in these polymers, is crucial in enhancing the charge transfer process and tuning the bandgap of the polymer via the substitution of various functional groups [86,92,99].

Conducting polymers can provide uniform coverage or encapsulation of MHP nanoparticles due to their good solubility in polar solvents through a reduced contact angle. Conjugated, moisture-resistant polymers like polyaniline can double up as protective layers and as charge-transport layers [86,92] when doped with organic acids. Protection through surface passivation and energy band alignment have been shown to be key to the improvement of the optoelectronic properties of MHP/polymer nanocomposites by promoting charge carrier transport. For instance, Yu and co-workers [100] demonstrated highly efficient MHP nanocrystal LEDs (PeNLEDs) with improved long-term stability prepared by the drop-casting method. Their study revealed that the $CsPbBr_3:PMMA$ composite film exhibited a maximum luminance of 637 cdm^{-2} (at 6.4 V) and an EQE of 0.25% (at 5.0 V) with a low turn-on voltage. The prepared composite film showed the formation of a monolayer of $CsPbBr_3$ nanocrystals without particle agglomeration. Further analysis of the PMMA matrix with the imbedded $CsPbBr_3$ nanocrystals revealed a uniform morphology, longer charge carrier lifetimes, and improved resistance to air exposure [100].

MHPs inherently possess a highly brittle crystal structure and exceedingly low cohesion energy and inevitably suffer from decreased fracture resistance and high mechanical instability. Research shows that the MHPs' structural deficiencies cannot be overcome by reducing surface and bulk defects, so external reinforcements of MHPs using poly-

mers could offer advantageous mechanical properties [79,82]. Incorporating MHPs within low-elastic moduli polymers has been found to allow for sufficient plastic deformation to dissipate strain or external mechanical energy under varied temperatures, which increases fracture energy [79,82]. Further, hydrophobic functional groups of some polymers prevent moisture and oxygen from accessing adsorption sites in MHPs to trigger structural and charge transport degradation, which may negatively affect the performance of devices like perovskite-based solar cells [79]. In MHP/polymer nanocomposites, specific spatial organization of MHP nanocrystals within the polymer matrix has been found to affect polymer-MHP nanocrystal interactions and significantly enhance not only the structural and mechanical properties but also the optical properties [79]. For instance, Xin and co-workers [78] successfully prepared CsPbBr₃-PMMA, CsPbBr₃-PBMA, and CsPbBr₃-PS composites with high and stable luminescence. Their study revealed that the prepared composites were highly luminescent, with excellent performance in the photoluminescence spectra and high PLQYs (>60%) for bulk materials.

Carrizo et al. (2021) [93] demonstrated lead halide perovskite-polymer nanocomposites prepared by casting or spin coating to produce a high fluorescence yield and a fully water-resistant material. The group successfully produced MAPbBr₃-HDA@PPGly/PSU films containing well-dispersed ~10 nm MAPbBr₃ nanocrystals that retained a bright green fluorescence emission even after eighteen months under air conditions or water immersion up to 45 °C. From water contact angle measurements, profilometry, and X-ray photoelectron spectroscopy data, it could be assumed that the slightly hydrophobic PSU polymer was responsible for the high water stability of the fluorescent films, which prevented MAPbBr₃-HDA nanocrystal degradation. Their work showed that the dispersion of the MAPbBr₃-HDA in dissolved commodity polymers holds great promise for the long-term stability of these composites for the future development of wearable electronic devices and other waterproof applications [93].

In PSCs, polymer additives have shown promising results in improving not only the PV cell efficiency but also the enhanced protection against environmental stressors. For instance, Jiang and colleagues [101] successfully demonstrated a high-performance polymer-doped MAPbI₃ perovskite in a PV device, as shown in Figure 9. The authors found that the long-chain polymer helps to form a network among the perovskite crystalline grains, leading to improved film morphology and device stability. The dewetting process was greatly suppressed by the cross-linking effect of the polymer chains, thereby resulting in uniform perovskite films with large grain sizes. Moreover, it was found that the polymer-doped perovskite shows a reduced trap-state density, likely due to the polymer effectively passivating the perovskite grain surface. Meanwhile, the doped polymer formed a bridge between grains for efficient charge transport. Using this approach, the PV cell efficiency was improved from 17.43% to as high as 19.19%, with significantly improved stability [101].

Besides the improved PV cell efficiency, incorporating MHPs into polymer matrices could result in enhanced protection against environmental stressors such as moisture and oxygen/air, thereby enhancing long-term PV device stability. Wang and co-workers (2016) [88] prepared a polymer-perovskite composite-based PV cell with increased performance stability. According to the study, the poly[[4,8-bis[(2-ethylhexyl)oxy]benzo[1,2-b:4,5-b']dithiophene-2,6-diyl][3-fluoro-2-[(2-ethylhexyl)carbonyl]thieno[3,4-b]thiophenediyl]] (PTB-7)-modified MAPbI₃ composite-based PV cell maintained its original open circuit voltage (V_{OC}) value after 920 h of storage, while the V_{OC} value for pristine perovskite PV cell started dipping after 360 h to ~90% of its original V_{OC} value after 528 h of storage, as seen in Figure 10a. The short circuit density (J_{SC}) of the PTB7-MAPbI₃ composite PV cells exhibited no change prior to the 528th hour and maintained ~93% of its original value after the 920th hour, while undoped PV cells showed a noticeable decline after 360 h and ~31% of their original value was observed after 528 h of storage (Figure 10b). Simultaneously, the PCEs of the PTB7-MAPbI₃ composite and undoped PV cell are recorded in Figure 10c. The PBT7-MAPbI₃ composite PV cell maintained ~92% and ~85% of the PCE values after 528 and 920 h of storage, respectively, while the undoped PV cell exhibited a decrease in

the PCE value to ~79% and ~21% after 168 and 528 h of storage. The fill factor (FF) of the PBT7-MAPbI₃ composite PV cell retained more than 90% of the original FF value, while the undoped PV cell FF value reduced to ~47% of its original value after 528 h of storage (Figure 10d). Therefore, one of the main factors in the degradation of the PV solar cells can be attributed to the decrease in J_{SC} that could be caused by the alternation or decomposition of perovskite material in the photoactive layer. The degradation of PBT7-MAPbI₃ composite and undoped PV cells was studied at ambient air and ~35% moisture content. The results show no significant changes in the V_{OC} value after 172 h of exposure. The J_{SC} , PCE, and FF values for both PV cells exhibited a gradual reduction with exposure. After 172 h of exposure, the PBT7-MAPbI₃ composite PV cell maintained ~68%, 64%, and 75% of the original J_{SC} , PCE, and FF values, respectively. While ~37%, 18%, and 43% of the J_{SC} , PCE, and FF, respectively, were preserved for the undoped PV device after the same period [88].

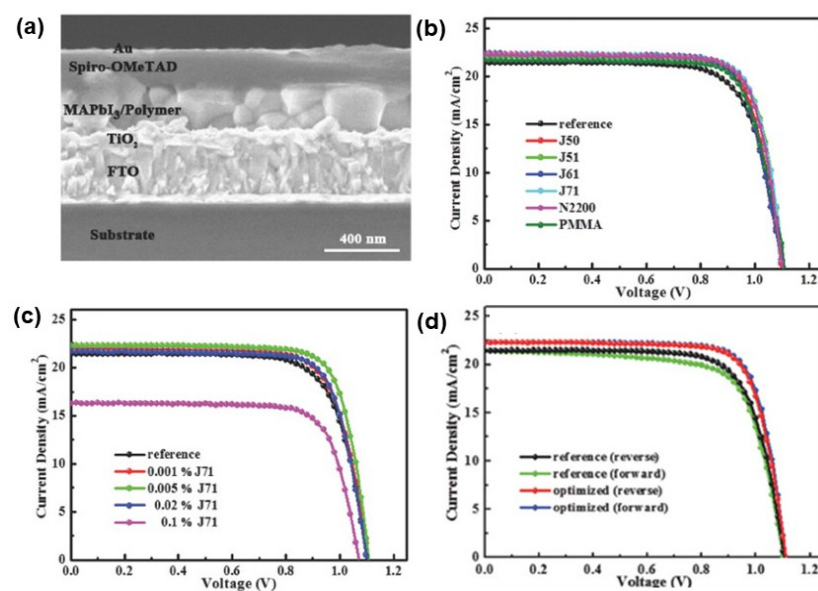


Figure 9. Polymer/perovskite nanocomposites as photoactive layers in PV cells: (a) cross-sectional scanning electron microscopy (SEM) micrograph of the polymer-perovskite nanocomposite-derived PV cell; (b) effect of different polymer additives on the PV cell performance; (c) effect of polymer loading on the PV cell performance; and (d) comparison between the undoped and optimized polymer-doped PV cells for both forward and reverse bias [101].

Similar observations were noted by the Han research group [87] in 2019. The group prepared polymeric Lewis-base-containing perovskite films with higher environmental stability. According to the data, the bare MAPbI₃ films exhibited severe decomposition under harsh environmental conditions (relative humidity, or RH, of $70 \pm 5\%$ for 150 h; light: AM 1.5 G for 2 h; and T: 100 °C in N₂ for 66 h), as Figure 11a–c. However, poly(propylene carbonate) (PPC, [C₄H₆O₃]_n)-modified MAPbI₃ films maintained relatively high amounts of the perovskite compared to that of bare MAPbI₃ films. A further increase in the polymer loading resulted in a significant decrease in the perovskite film degradation. Residue polymeric Lewis bases in the perovskite films could also be effective in passivating the defect sites at grain boundaries with high-binding energies. The improved environmental stability can be attributed to the addition of the PPC and its inter-granular cross-linking phenomenon, which minimizes the inter-granular electrical decoupling. Moreover, the PV cell performances of the cross-linked PPC-modified PSCs exhibited significantly superior resistance against similar harsh environmental conditions. As a result, all the PV cell parameters of the devices, including J_{SC} , V_{OC} , and FF, were enhanced, and the highest PCE of 20.06% (stabilized efficiency of 19.48%) was achieved alongside significantly improved ambient and operational stability, as denoted in Figure 11d–f [87].

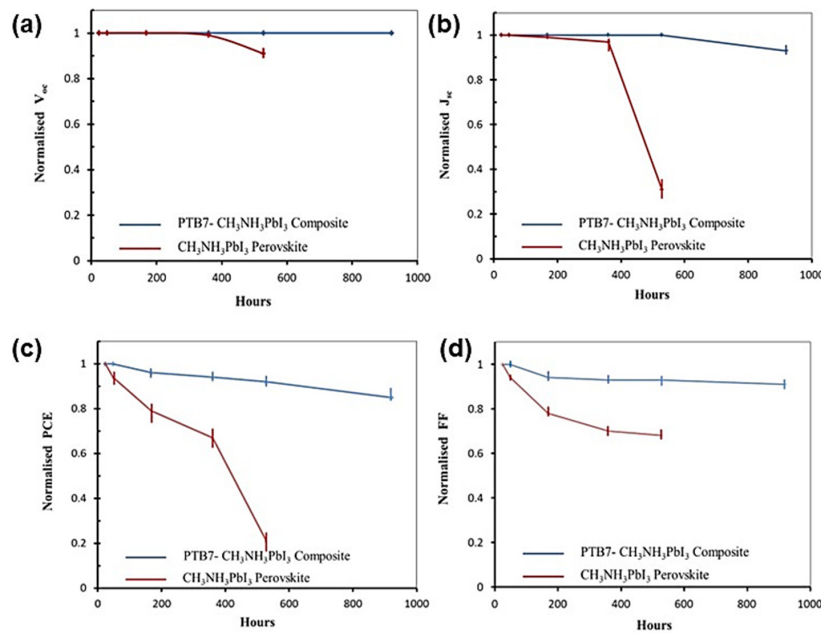


Figure 10. Performance variation of the undoped and PBT7-perovskite PV cells stored in the glovebox against time: (a) V_{oc} measurements; (b) J_{sc} measurements; (c) PCE measurements; and (d) FF measurements [88].

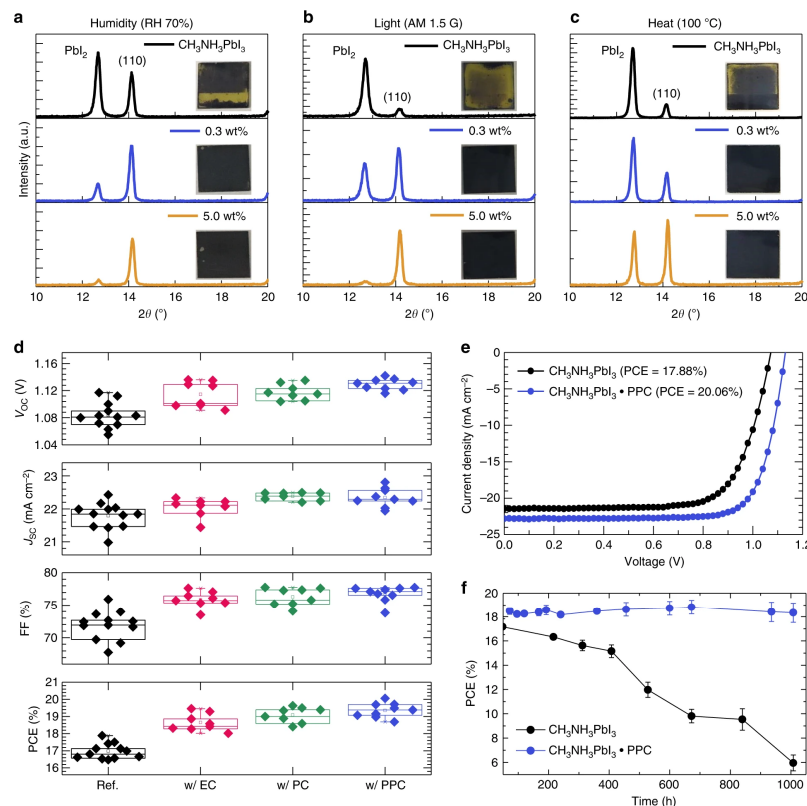


Figure 11. Environmental stability and photovoltaic performances. XRD spectra of bare MAPbI₃ and PPC-MAPbI₃ films against: (a) moisture (RH: 70 ± 5%); (b) light (AM 1.5 G); and (c) heat (100 °C); (d) photovoltaic parameters of PSCs with the addition of different polymeric Lewis bases: J_{sc} , V_{oc} , FF, and PCE. Each box chart includes the minimum, lower quartile (lower horizontal line), median (middle horizontal line), mean (hollow square), upper quartile (upper horizontal line), maximum, and discrete data; (e) current density–voltage (I – V) characteristics; and (f) PCE evolution in ambient conditions as a function of time of MAPbI₃-based solar cells without and with PPC [87].

Polymer-modified perovskite nanocomposites have also shown remarkable long-term performance stability, making these materials very important in not only PV cells but also in the development of LEDs due to their high color purity, tunable band gap, low nonradiative recombination rates, and high electron-hole mobility [80,102]. For instance, Cai and colleagues [102] demonstrated an efficient LED with pure-red emission based on polymer-assisted in-situ growth of high-quality all-inorganic $\text{CsPbBr}_{0.6}\text{I}_{2.4}$ perovskite nanocrystal films with a homogenous distribution of nanocrystals with sizes 20–30 nm, as shown in Figure 12a–c. With this method, we can dramatically reduce the formation temperature of $\text{CsPbBr}_{0.6}\text{I}_{2.4}$ and stabilize its perovskite phase. Eventually, the team successfully demonstrated a pure-red-emission perovskite light-emitting diode (PeLED) with a high external quantum efficiency (EQE) of 6.55% and luminance of 338 cd/m^2 . Furthermore, the device obtains an ultralow turn-on voltage of 1.5 V and a half-lifetime of over 0.5 h at a high initial luminance of 300 cd/m^2 .

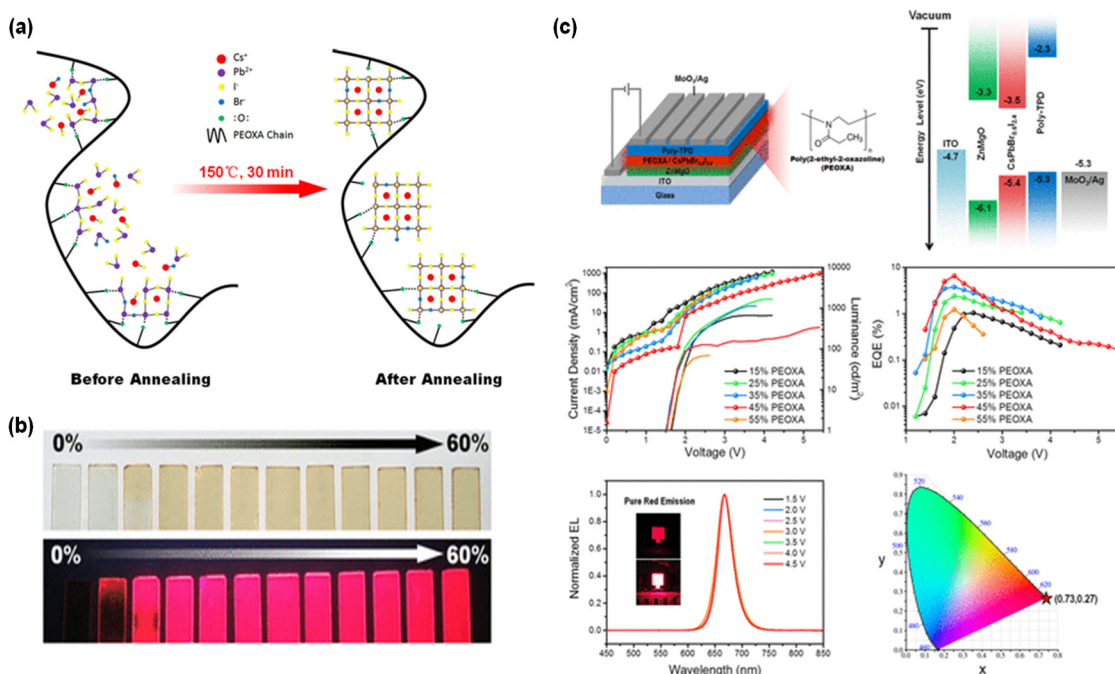


Figure 12. (a) Schematic diagram of polymer-induced in situ perovskite nanocrystal formation process; (b) photos of $\text{CsPbBr}_{0.6}\text{I}_{2.4}$ thin films with various concentrations of PEOXA under daylight (upper one) and UV light (below one); (c) LED performance of the PEOXA- $\text{CsPbBr}_{0.6}\text{I}_{2.4}$ thin films. [102].

Polymer-perovskite nanocomposites improve long-term photoluminescence stability against environmental stressors. For instance, Su and colleagues [80] prepared a CsPbBr_3 PNC/polymer composite by PNC dispersion and UV-induced chemical crosslinking, as shown in Figure 13. The optimal poly₂/ CsPbBr_3 PNCs composite film showed a high PLQY of 82% comparable to CsPbBr_3 PNCs suspension, along with a high surface superhydrophobicity. This film exhibited a high PL intensity (90% of the original value) after air-aging for 60 days. Its surface superhydrophobicity was attributed to the use of VT-PDMS monomers for achieving high micro-nano surface roughness and low thin-film surface energy. A white-LED device was well built using this optimal poly₂/ CsPbBr_3 composite film, and its color coordinates (0.343, 0.334) can be close to standard white light. The promising backlight display application of the optimal film was verified. The innovation of the current study is the simultaneously-achieved high PL and surface hydrophobic properties of composites. This study will provide a simple approach for improving the PL stability of PNCs by preparing polymer-based composite films with high surface hydrophobicity for modern LED devices [80].

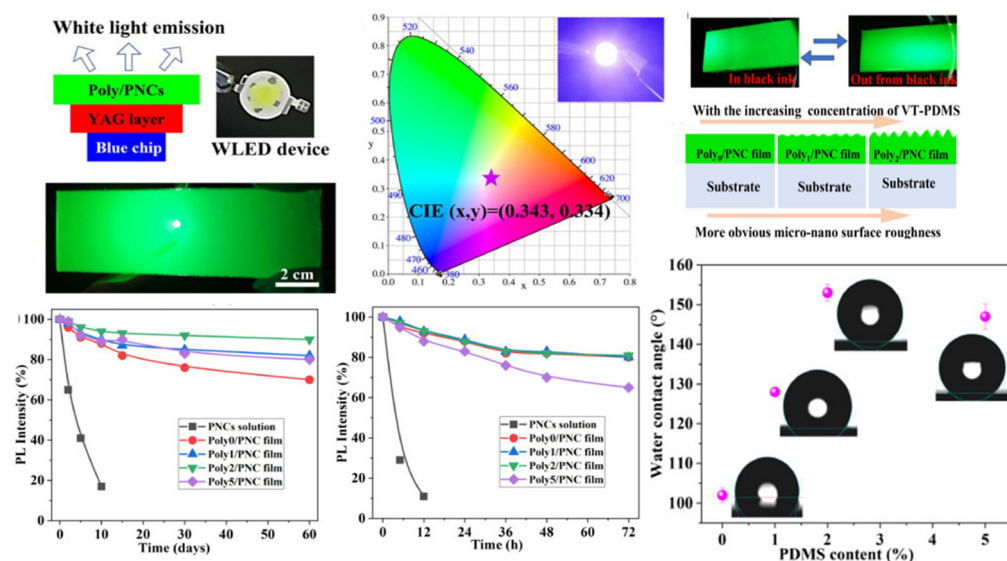


Figure 13. Schematic diagram of a polymer/CsPbBr₃ PNCs nanocomposite-based white LED device, including PL performance over a period of time, wet contact angle vs. PDMS content, and CIE coordinates [80].

5. Conclusions and Future Perspectives

In conclusion, this review highlights the distinctive characteristics of halide perovskite materials that have made them topical materials in the fields of photovoltaics and optoelectronics. The major stumbling blocks to the realization of commercial devices from these materials are briefly described, leading to the discussion of environmentally resistant device materials and/or architectures. More specifically, this discussion zooms in on recent progress in the preparation of MHP/polymer nanocomposites to minimize the perovskite's susceptibility to environmental factors such as moisture, air/oxygen, UV radiation, and heat. Passivation of the perovskite component by the polymer and the hydrophobic nature of most polymers are some of the desirable properties that the nanocomposite inherits from the synergistic combination of the two materials. It has been demonstrated that the charge transport properties (e.g., carrier lifetime) of the nanocomposite materials improve through, for example, the annihilation of defect trap centers through surface passivation. Band alignment when using conjugate polymers is another way in which the lifetime of charge carriers is enhanced. Other notable changes that the review makes mention of include enhanced luminescence stability and improved moisture resistance.

Despite the rapid growth in this field, several issues still need to be elucidated. For instance, most polymers are non-conducting by nature and may have a negative effect on the overall optoelectronic properties of MHPs. Hence, the composition and molecular weight of the polymer become important parameters for the manipulation of the interactions and self-assembly of MHP-NCs. Where non-conducting polymers are used, it may be advisable to use the polymer purely as an encapsulating matrix. One way of doing this could be to grow nanowires of the perovskite active layer inside ion-track-etched membranes of the polymer material. Continued progress in the synthesis and fundamental understanding of the composition-structure-property relationships of different device architectures may open new avenues for widespread applications of MHP-NC/polymer nanocomposites in PSCs, LEDs, and PDs. It is hoped that this review adds to the contemporary discourse aimed at the development of efficient, low-cost photovoltaic devices and systems based on MHP-NC/polymer nanocomposites.

Author Contributions: Conceptualization, M.A.M. and M.M.; methodology, M.A.M.; software, M.A.M.; validation, M.A.M. and M.M.; formal analysis, M.A.M.; investigation, M.A.M.; resources, M.A.M.; data curation, M.A.M.; writing—original draft preparation, M.A.M.; writing—review and editing, M.A.M. and M.M.; visualization, M.A.M.; supervision, M.M.; project administration,

M.M.; funding acquisition, M.M. All authors have read and agreed to the published version of the manuscript.

Funding: This research received no external funding.

Data Availability Statement: No new data were created during the construction of the manuscript.

Acknowledgments: The authors gratefully acknowledge the Tshwane University of Technology for financial and administrative support through the Photovoltaic Nanocomposites R&D Platform, and NRF-iThemba Laboratory for Accelerator Based Sciences (LABS) for infrastructural support.

Conflicts of Interest: The authors declare no conflict of interest. The funders had no role in the design of the study; in the collection, analyses, or interpretation of data; in the writing of the manuscript; or in the decision to publish the results.

References

1. Zhang, J.; Li, X.; Wang, L.; Yu, J.; Wageh, S.; Al-Ghamdi, A.A. Enhanced performance of $\text{CH}_3\text{NH}_3\text{PbI}_3$ perovskite solar cells by excess halide modification. *Appl. Surf. Sci.* **2021**, *564*, 150464. [[CrossRef](#)]
2. Nishimura, K.; Kamarudin, M.A.; Hirotani, D.; Hamada, K.; Shen, Q.; Iikubo, S.; Minemoto, T.; Yoshino, K.; Hayase, S. Lead-free tin-halide perovskite solar cells with 13% efficiency. *Nano Energy* **2020**, *74*, 104858. [[CrossRef](#)]
3. Ahmad, K.; Kim, H. Improved photovoltaic performance and stability of perovskite solar cells with device structure of (ITO/SnO₂/CH₃NH₃PbI₃/rGO+spiro-MeOTAD/Au). *Mater. Sci. Eng. B* **2023**, *289*, 116227. [[CrossRef](#)]
4. De Franco, M.; Cirignano, M.; Cavattoni, T.; Jalali, H.B.; Prato, M.; Di Stasio, F. Facile purification protocol of CsPbBr₃ nanocrystals for light-emitting diodes with improved performance. *Opt. Mater. X* **2022**, *13*, 100124. [[CrossRef](#)]
5. Iskandar, J.; Lee, C.-C.; Kurniawan, A.; Cheng, H.-M.; Liu, S.-W.; Biring, S. Improving the efficiency of near-IR perovskite LEDs via surface passivation and ultrathin interfacial layers. *Cell Rep. Phys. Sci.* **2022**, *3*, 101170. [[CrossRef](#)]
6. Kim, B.W.; Heo, J.H.; Park, J.K.; Lee, D.S.; Park, H.; Kim, S.Y.; Kim, J.H.; Im, S.H. Morphology controlled nanocrystalline CsPbBr₃ thin-film for metal halide perovskite light emitting diodes. *J. Ind. Eng. Chem.* **2021**, *97*, 417–425. [[CrossRef](#)]
7. Ding, J.; Cheng, X.; Jing, L.; Zhou, T.; Zhao, Y.; Du, S. Polarization-dependent optoelectronic performances in hybrid halide perovskite MAPbX₃ (X = Br, Cl) single-crystal photodetectors. *ACS Appl. Mater. Interfaces* **2018**, *10*, 845–850. [[CrossRef](#)]
8. Li, Z.; Li, H.; Jiang, K.; Ding, D.; Li, J.; Ma, C.; Jiang, S.; Wang, Y.; Anthopoulos, T.D.; Shi, Y. Self-powered perovskite/CdS heterostructure photodetectors. *ACS Appl. Mater. Interfaces* **2019**, *11*, 40204–40213. [[CrossRef](#)]
9. Cheng, Z.; Liu, K.; Yang, J.; Chen, X.; Xie, X.; Li, B.; Zhang, Z.; Liu, L.; Shan, C.; Shen, D. High-performance planar-type ultraviolet photodetector based on high-quality CH₃NH₃PbCl₃ perovskite single crystals. *ACS Appl. Mater. Interfaces* **2019**, *11*, 34144–34150. [[CrossRef](#)]
10. Kojima, A.; Teshima, K.; Shirai, Y.; Miyasaka, T. Organometal halide perovskites as visible-light sensitizers for photovoltaic cells. *J. Am. Chem. Soc.* **2009**, *131*, 6050–6051. [[CrossRef](#)]
11. Interactive Best Research—Cell Efficiency Chart, NREL. Available online: <https://www.nrel.gov/pv/assets/pdfs/cell-pv-eff-emergingpv.pdf> (accessed on 29 September 2023).
12. Pham, H.D.; Yang, T.C.-J.; Jain, S.M.; Wilson, G.J.; Sonar, P. Development of dopant-free organic hole transporting materials for perovskite solar cells. *Adv. Energy Mater.* **2020**, *10*, 1903326. [[CrossRef](#)]
13. Im, J.-H.; Lee, C.-R.; Lee, J.-W.; Park, S.-W.; Park, N.-G. 6.5% efficient perovskite quantum-dot-sensitized solar cell. *Nanoscale* **2011**, *3*, 4088–4093. [[CrossRef](#)] [[PubMed](#)]
14. Lee, M.M.; Teuscher, J.; Miyasaka, T.; Murakami, T.N.; Snaith, H.J. Efficient hybrid solar cells based on meso-superstructured organometal halide perovskites. *Science* **2012**, *338*, 643–647. [[CrossRef](#)] [[PubMed](#)]
15. Burschka, J.; Pellet, N.; Moon, S.-J.; Humphry-Baker, R.; Gao, P.; Nazeeruddin, M.K.; Grätzel, M. Sequential deposition as a route to high-performance perovskite-sensitized solar cells. *Nature* **2013**, *499*, 316–319. [[CrossRef](#)] [[PubMed](#)]
16. Jeon, N.J.; Noh, J.H.; Yang, W.S.; Kim, Y.C.; Ryu, S.; Seo, J.; Seok, S.I. Compositional engineering of perovskite materials for high-performance solar cells. *Nature* **2015**, *517*, 476–480. [[CrossRef](#)]
17. Jiang, Q.; Zhao, Y.; Zhang, X.; Yang, X.; Chen, Y.; Chu, Z.; Ye, Q.; Li, X.; Yin, Z.; You, J. Surface passivation of perovskite film for efficient solar cells. *Nat. Photonics* **2019**, *13*, 460–466. [[CrossRef](#)]
18. Kim, G.; Min, H.; Lee, K.S.; Lee, D.Y.; Yoon, S.M.; Seok, S.I. Impact of strain relaxation lead iodide perovskite solar cells. *Science* **2020**, *370*, 108–112. [[CrossRef](#)]
19. Jeong, J.; Kim, M.; Seo, J.; Lu, H.; Ahlawat, P.; Mishra, A.; Yang, Y.; Hope, M.A.; Eickemeyer, F.T.; Kim, M.; et al. Pseudo-halide anion engineering for α -FAPbI₃ perovskite solar cells. *Nature* **2021**, *592*, 381–385. [[CrossRef](#)]
20. De Wolf, S.; Holovsky, J.; Moon, S.-J.; Löper, P.; Niesen, B.; Ledinsky, M.; Haug, F.-J.; Yum, J.-H.; Ballif, C. Organometallic halide perovskites: Sharp optical absorption edge and its relation to photovoltaic performance. *J. Phys. Chem. Lett.* **2014**, *5*, 1035–1039. [[CrossRef](#)]
21. Pellet, N.; Gao, P.; Gregori, G.; Yang, T.-Y.; Nazeeruddin, M.K.; Maier, J.; Grätzel, M. Mixed-organic-cation perovskite photovoltaics for enhanced solar-light harvesting. *Angew. Chem. Int. Ed.* **2014**, *53*, 3151–3157. [[CrossRef](#)]

22. Liu, X.-Y.; Cui, Y.; Deng, J.-P.; Liu, Y.-Y.; Ma, X.-F.; Hou, Y.-X.; Wei, J.-Y.; Li, Z.-Q.; Wang, Z.-W. Charge carriers trapping by the full-configuration defects in metal halide perovskites quantum dots. *J. Phys. Chem. Lett.* **2022**, *13*, 8858–8863. [[CrossRef](#)]
23. Targhi, F.F.; Jalili, Y.S.; Kanjouri, F. MAPbI₃ and FAPbI₃ perovskites as solar cells: Case study on structural, electrical and optical properties. *Res. Phys.* **2018**, *10*, 616–627. [[CrossRef](#)]
24. Chen, X.; Peng, L.; Huang, K.; Shi, Z.; Xie, R.; Yang, W. Non-injection gram-scale synthesis of cesium lead halide perovskite quantum dots with controllable size and composition. *Nano Res.* **2016**, *9*, 1994–2006. [[CrossRef](#)]
25. Mandal, A.; Ghosh, A.; Ghosh, D.; Bhattacharyya, S. Photodetectors with high responsivity by thickness tunable mixed halide perovskite nanosheets. *ACS Appl. Mater. Interfaces* **2021**, *13*, 43104–43114. [[CrossRef](#)]
26. Huang, L.; Gao, Q.; Sun, L.-D.; Dong, H.; Shi, S.; Cai, T.; Liao, Q.; Yan, C.-H. Composition-graded cesium lead halide perovskite nanowires with tunable dual-color lasing performance. *Adv. Mater.* **2018**, *30*, 1800596. [[CrossRef](#)] [[PubMed](#)]
27. Lai, M.; Kong, Q.; Bischak, C.-G.; Yu, Y.; Dou, L.; Eaton, S.W.; Ginsberg, N.S.; Yang, P. Structural, optical, and electrical properties of phase-controlled cesium lead iodide nanowires. *Nano Res.* **2017**, *10*, 1107–1114. [[CrossRef](#)]
28. Wali, Q.; Iftikhar, F.J.; Khan, M.E.; Ullah, A.; Iqbal, Y.; Jose, R. Advances in stability of perovskite solar cells. *Org. Elect.* **2020**, *78*, 105590. [[CrossRef](#)]
29. Thomas, S. Observing phase transitions in a halide perovskite using temperature dependent photoluminescence spectroscopy. In *Edinburgh Instrument Application Note*; Edinburgh Instruments Ltd.: Livingston, UK, 2018.
30. Kim, H.-S.; Im, S.H.; Park, N.-G. Organolead halide perovskite: New horizons in solar cell research. *J. Phys. Chem. C* **2014**, *118*, 5615–5625. [[CrossRef](#)]
31. Ali, H.M.; Reda, S.M.; Ali, A.I.; Mousa, M.A. A quick peek at solar cells and a closer insight at perovskite solar cells. *Egypt. J. Pet.* **2021**, *30*, 53–63. [[CrossRef](#)]
32. Leijtens, T.; Eperon, G.E.; Noel, N.K.; Haberreutinger, S.N.; Petrozza, A.; Snaith, H.J. Stability of metal halide perovskite solar cells. *Adv. Energy Mater.* **2015**, *5*, 1500963. [[CrossRef](#)]
33. Li, J.; Chen, Z.; Saha, S.; Utterback, J.K.; Aubrey, M.L.; Yuan, R.; Weaver, H.L.; Ginsberg, N.S.; Chapman, K.W.; Filip, M.R.; et al. Zwitterions in 3D perovskites: Organosulfide-halide perovskites. *J. Am. Chem. Soc.* **2022**, *144*, 22403–22408. [[CrossRef](#)] [[PubMed](#)]
34. Goldschmidt, V.M. Krystallbau und chemische zusammensetzung. *Berichte Dtsch. Chem. Ges. A/B* **1927**, *60*, 1263–1296. [[CrossRef](#)]
35. Yang, W.F.; Igbari, F.; Lou, Y.-H.; Wang, Z.-K.; Liao, L.-S. Tin halide perovskites: Progress and challenges. *Adv. Energy Mater.* **2020**, *10*, 1902584. [[CrossRef](#)]
36. Li, C.; Lu, X.; Ding, W.; Feng, L.; Gao, Y.; Guo, Z. Formability of ABX₃ (X = F, Cl, Br, I) halide perovskites. *Acta Cryst. B* **2008**, *B64*, 702–707. [[CrossRef](#)] [[PubMed](#)]
37. Han, T.-H.; Tan, S.; Xue, J.; Meng, L.; Lee, J.-W.; Yang, Y. Interface and defect engineering for metal halide perovskite optoelectronic devices. *Adv. Mater.* **2019**, *31*, 1803515. [[CrossRef](#)] [[PubMed](#)]
38. Nasti, G.; Abate, A. Tin halide perovskite (ASnX₃) solar cells: A comprehensive guide toward the highest power conversion efficiency. *Adv. Energy Mater.* **2020**, *10*, 1902467. [[CrossRef](#)]
39. Travis, W.; Glover, E.N.K.; Bronstein, H.; Scanlon, D.O.; Palgrave, R.G. On the application of the tolerance factor to inorganic and hybrid halide perovskites: A revised system. *Chem. Sci.* **2016**, *7*, 4548–4556. [[CrossRef](#)]
40. Hussain, I.; Tran, H.P.; Jaksik, J.; Moore, J.; Islam, N.; Uddin, M.J. Functional materials, device architecture, and flexibility of perovskite solar cell. *Emergent Mater.* **2018**, *1*, 133–154. [[CrossRef](#)]
41. Aftab, A.; Ahmad, I. A review of stability and progress in tin halide perovskite solar cell. *Sol. Energy* **2021**, *216*, 26–47. [[CrossRef](#)]
42. Hong Noh, J.; Im, S.H.; Heo, J.H.; Mandal, N.; Seok, S.I. Chemical management for colorful, efficient, and stable inorganic–organic hybrid nanostructured solar cells. *Nano Lett.* **2013**, *13*, 1764–1769.
43. Protesescu, L.; Yakunin, S.; Bodnaruk, M.I.; Krieg, F.; Caputo, R.; Hendon, C.H.; Yang, R.X.; Walsh, A.; Kovalenko, M.V. Nanocrystals of cesium lead halide perovskites (CsPbX₃, X = Cl, Br, and I): Novel optoelectronic materials showing bright emission with wide color gamut. *Nano Lett.* **2015**, *15*, 3692–3696. [[CrossRef](#)] [[PubMed](#)]
44. Tao, S.X.; Cao, X.; Bobbert, P.A. Accurate and efficient band gap predictions of metal halide perovskites using the DFT-1/2 method: GW accuracy with DFT expense. *Sci. Rep.* **2017**, *7*, 14386. [[CrossRef](#)] [[PubMed](#)]
45. Ye, X.; Liu, A.; Zhao, Y.; Han, Q.; Kitamura, T.; Ma, T. DFT study of X-site ion substitution doping of Cs₂PtX₆ on its structural and electronic properties. *Int. J. Energy Res.* **2022**, *46*, 8471–8479. [[CrossRef](#)]
46. Rasukkannu, M.; Velauthapillai, D.; Vajeeston, P. A first-principle study of the electronic, mechanical and optical properties of inorganic perovskite Cs₂SnI₆ for intermediate-band solar cells. *Mater. Lett.* **2018**, *218*, 233–236. [[CrossRef](#)]
47. Ornelas-Cruz, I.; Trejo, A.; Oviedo-Roa, R.; Salazar, F.; Carvajal, E.; Miranda, A.; Cruz-Irisson, M. DFT-based study of the bulk tin mixed-halide CsSnI_{3-x}Br_x perovskite. *Comput. Mater. Sci.* **2020**, *178*, 109619. [[CrossRef](#)]
48. RaeisianAsl, M.; Panahi, S.F.K.S.; Jamaati, M.; Tafreshi, S.S. A review on theoretical studies of structural and optoelectronic properties of FA-based perovskite materials with a focus on FAPbI₃. *Int. J. Energy Res.* **2022**, *46*, 13117–13151. [[CrossRef](#)]
49. Tao, S.; Schmidt, I.; Brocks, G.; Jiang, J.; Tranca, I.; Meerholz, K.; Olthof, S. Absolute energy level positions in tin and lead-based halide perovskites. *Nat. Commun.* **2019**, *10*, 2560. [[CrossRef](#)]
50. Nishat, M.; Hossain, K.; Hossain, R.; Khanom, S.; Ahmed, F.; Hossain, A. Role of metal and anions in organo-metal halide perovskites CH₃NH₃MX₃ (M: Cu, Zn, Ga, Ge, Sn, Pb; X: Cl, Br, I) on structural and optoelectronic properties for photovoltaic applications. *RSC Adv.* **2022**, *12*, 13281–13294. [[CrossRef](#)]

51. Stoumpos, C.C.; Malliakas, C.D.; Kanatzidis, M.G. Semiconducting tin and lead iodide perovskites with organic cations: Phase transitions, high mobilities, and near-infrared photoluminescent properties. *Inorg. Chem.* **2013**, *52*, 9019–9038. [CrossRef]
52. Chung, I.; Song, J.-H.; Im, J.; Androulakis, J.; Malliakas, C.D.; Li, H.; Freeman, A.J.; Kenney, J.T.; Kanatzidis, M.G. CsSnI₃: Semiconductor or metal? high electrical conductivity and strong near-infrared photoluminescence from a single material. High hole mobility and phase-transitions. *J. Am. Chem. Soc.* **2012**, *134*, 8579–8587. [CrossRef]
53. Stoumpos, C.C.; Kanatzidis, M.G. Halide perovskites: Poor man’s high-performance semiconductors. *Adv. Mater.* **2016**, *28*, 5778–5793. [CrossRef] [PubMed]
54. Dong, Q.; Fang, Y.; Shao, Y.; Mulligan, P.; Qiu, J.; Cao, L.; Huang, J. Electron-hole diffusion lengths > 175 μm in solution-grown CH₃NH₃PbI₃ single crystals. *Science* **2015**, *347*, 967–970. [CrossRef] [PubMed]
55. Valverde-Chávez, D.A.; Poncea, C.S., Jr.; Stoumpos, C.C.; Yartsev, A.; Kanatzidis, M.G.; Sundström, V.; Cooke, D.G. Intrinsic femtosecond charge generation dynamics in single crystal CH₃NH₃PbI₃. *Energy Environ. Sci.* **2015**, *8*, 3700–3707. [CrossRef]
56. Zhang, J.; Yu, C.; Wang, L.; Li, Y.; Ren, Y.; Shum, K. Energy barrier at the N719-dye/CsSnI₃ interface for photogenerated holes in dye-sensitized solar cells. *Sci. Rep.* **2014**, *4*, 6954. [CrossRef]
57. Yuan, Y.; Huang, J. Ion migration in organometal trihalide perovskite and its impact on photovoltaic efficiency and stability. *Acc. Chem. Res.* **2016**, *49*, 286–293. [CrossRef]
58. Yin, W.-J.; Shi, T.; Yan, Y. Unusual defect physics in CH₃NH₃PbI₃ perovskite solar cell absorber. *Appl. Phys. Lett.* **2014**, *104*, 063903. [CrossRef]
59. Niu, T.; Xue, Q.; Yip, H.-L. Molecularly Engineered Interfaces in Metal Halide Perovskite Solar Cells. *J. Phys. Chem. Lett.* **2021**, *12*, 4882–4901. [CrossRef]
60. Hoke, E.T.; Slotcavage, D.J.; Dohner, E.R.; Bowring, A.R.; Karunadasa, H.I.; McGehee, M.D. Reversible photo-induced trap formation in mixed-halide hybrid perovskites for photovoltaics. *Chem. Sci.* **2015**, *6*, 613–617. [CrossRef]
61. Boyd, C.C.; Cheacharoen, R.; Leijtens, T.; McGehee, M.D. Understanding degradation mechanisms and improving stability of perovskite photovoltaics. *Chem. Rev.* **2019**, *119*, 3418–3451. [CrossRef]
62. Kulbak, M.; Gupta, S.; Kedem, N.; Levine, I.; Bendikov, T.; Hodes, G.; Cahen, D. Cesium enhances long-term stability of lead bromide perovskite-based solar cells. *J. Phys. Chem. Lett.* **2016**, *7*, 167–172. [CrossRef]
63. Frost, J.M.; Butler, K.T.; Brivio, F.; Hendon, C.H.; van Schilfgaarde, M.; Walsh, A. Atomistic origins of high-performance in hybrid halide perovskite solar cells. *Nano Lett.* **2014**, *14*, 2584–2590. [CrossRef] [PubMed]
64. Pearson, A.J.; Eperon, G.E.; Hopkinson, P.E.; Haberstroh, S.N.; Wang, J.T.-W.; Snaith, H.J.; Greenham, N.C. Oxygen degradation in mesoporous Al₂O₃/CH₃NH₃PbI_{3-x}Cl_x perovskite solar cells: Kinetics and mechanisms. *Adv. Energy Mater.* **2016**, *6*, 1600014. [CrossRef]
65. Bryant, D.; Aristidou, N.; Pont, S.; Sanchez-Molina, I.; Chotchunangatchaval, T.; Wheeler, S.; Durrant, J.R.; Haque, S.A. Light and oxygen induced degradation limits the operational stability of methylammonium lead triiodide perovskite solar cells. *Energy Environ. Sci.* **2016**, *9*, 1655–1660. [CrossRef]
66. Noel, N.K.; Stranks, S.D.; Abate, A.; Wehrenfennig, C.; Guarnera, S.; Haghimirad, A.-A.; Sadhanala, A.; Eperon, G.E.; Pathak, S.K.; Johnston, M.B.; et al. Lead-free organic–inorganic tin halide perovskites for photovoltaic applications. *Energy Environ. Sci.* **2014**, *7*, 3061–3068. [CrossRef]
67. Leijtens, T.; Eperon, G.E.; Pathak, S.; Abate, A.; Lee, M.M.; Snaith, H.J. Overcoming ultraviolet light instability of sensitized TiO₂ with meso-superstructured organometal tri-halide perovskite solar cells. *Nat. Commun.* **2013**, *4*, 2885. [CrossRef] [PubMed]
68. Pisoni, A.; Jaćimović, J.; Barišić, O.S.; Spina, M.; Gaál, R.; Forró, L.; Horváth, E.J. Ultra-low thermal conductivity in organic–inorganic hybrid perovskite CH₃NH₃PbI₃. *Phys. Chem. Lett.* **2014**, *5*, 2488–2492. [CrossRef] [PubMed]
69. Jeon, N.J.; Noh, J.H.Y.C.; Kim, Y.C.; Yang, W.S.; Ryu, S.; Seok, S.I. Solvent engineering for high-performance inorganic–organic hybrid perovskite solar cells. *Nat. Mater.* **2015**, *13*, 897–903. [CrossRef]
70. Jørgensen, M.; Norrman, K.; Gevorgyan, S.A.; Tromholt, T.; Andreassen, B.; Krebs, F.C. Stability of polymer solar cells. *Adv. Mater.* **2012**, *24*, 580–612. [CrossRef]
71. Bailie, C.D.; Unger, E.L.; Zakeeruddin, S.M.; Grätzel, M.; McGehee, M.D. Melt-infiltration of spiro-OMeTAD and thermal instability of solid-state dye-sensitized solar cells. *Phys. Chem. Chem. Phys.* **2014**, *16*, 4864–4870. [CrossRef]
72. Malinauskas, T.; Tomkute-Luksiene, D.; Sens, R.; Daskeviciene, M.; Send, R.; Wonneberger, H.; Jankauskas, V.; Bruder, I.; Getautis, V. Enhancing thermal stability and lifetime of solid-state dye-sensitized solar cells via molecular engineering of the hole-transporting material spiro-OMeTAD. *ACS Appl. Mater. Interfaces* **2015**, *7*, 11107–11116. [CrossRef]
73. Jena, A.K.; Ikegami, M.; Miyasaka, T. Severe morphological deformation of spiro-OMeTAD in (CH₃NH₃)PbI₃ solar cells at high temperature. *ACS Energy Lett.* **2017**, *2*, 1760–1761. [CrossRef]
74. Ferdowsi, P.; Ochoa-Martinez, E.; Alonso, S.S.; Steiner, U.; Saliba, M. Ultrathin polymeric films for interfacial passivation in wide band-gap perovskite solar cells. *Sci. Rep.* **2020**, *10*, 22260. [CrossRef] [PubMed]
75. Zhao, P.; Kim, B.J.; Jung, H.S. Passivation in perovskite solar cells: A review. *Mater. Today Energy* **2018**, *7*, 267–286. [CrossRef]
76. Wang, X.; Lian, X.; Zhang, Z.; Gao, H. Could nanocomposites continue the success of halide perovskites? *ACS Energy Lett.* **2019**, *4*, 1446–1454. [CrossRef]
77. Li, J.; Bu, T.; Lin, Z.; Mo, Y.; Chai, N.; Gao, X.; Ji, M.; Zhang, X.-L.; Cheng, Y.-B.; Huang, F. Efficient and stable perovskite solar cells via surface passivation of an ultrathin hydrophobic organic molecular layer. *Chem. Eng. J.* **2021**, *405*, 126712. [CrossRef]

78. Xin, Y.; Zhao, H.; Zhang, J. Highly stable and luminescent perovskite–polymer composites from a convenient and universal strategy. *ACS Appl. Mater. Interfaces* **2018**, *10*, 4971–4980. [[CrossRef](#)]
79. Su, P.; Huang, Y.; Li, Y.; Hu, C.; Shi, W. Improving photoluminescent water-stability of CsPbBr₃ perovskite nanocrystals via constructing nanocrystals/polymer composites with hydrophobic surfaces for LED applications. *Surf. Interfaces* **2023**, *37*, 102719. [[CrossRef](#)]
80. Wang, Z.; Fu, R.; Li, F.; Xie, H.; He, P.; Sha, Q.; Tang, Z.; Wang, N.; Zhong, H. One-step polymeric melt encapsulation method to prepare CsPbBr₃ perovskite quantum dots/polymethyl methacrylate composite with high performance. *Adv. Funct. Mater.* **2021**, *31*, 2010009. [[CrossRef](#)]
81. Kim, H.-J.; Oh, H.; Kim, T.; Kim, D.; Park, M. Stretchable photodetectors based on electrospun polymer/perovskite composite nanofibers. *ACS Appl. Nano Mater.* **2022**, *5*, 1308–1316. [[CrossRef](#)]
82. Bkkar, M.A.; Olekhnovich, R.O.; Uspenskaya, M.V. Perovskite-polymer nanocomposites based on nanofibers for flexible solar cells. In Proceedings of the International Conference Laser Optics (ICLO), Saint Petersburg, Russia, 21–24 June 2022.
83. Manshor, N.A.; Wali, Q.; Wong, K.K.; Muzakir, S.K.; Fakharuddin, A.; Schmidt-Mende, L.; Jose, R. Humidity versus photo-stability of metal halide perovskite films in a polymer matrix. *Phys. Chem. Chem. Phys.* **2016**, *18*, 21629–21639. [[CrossRef](#)]
84. Panda, S.; Soni, A.; Gupta, V.; Niranjan, R.; Panda, D. PVDF-directed synthesis, stability and anion exchange of cesium lead bromide nanocrystals. *Methods Appl. Fluoresc.* **2022**, *10*, 044005. [[CrossRef](#)]
85. Marques, A.S.; Szostak, R.; Marchezi, P.E.; Nogueira, A.F. Perovskite solar cells based on polyaniline derivatives as hole transport materials. *J. Phys. Energy* **2019**, *1*, 015004. [[CrossRef](#)]
86. Mei, Y.; Shen, Z.; Kundu, S.; Dennis, E.; Pang, S.; Tan, F.; Yue, G.; Gao, Y.; Dong, C.; Liu, R.; et al. Perovskite solar cells with polyaniline hole transport layers surpassing a 20% power conversion efficiency. *Chem. Mater.* **2021**, *33*, 4679–4687. [[CrossRef](#)]
87. Han, T.-H.; Lee, J.-W.; Choi, C.; Tan, S.; Lee, C.; Zhao, Y.; Dai, Z.; De Marco, N.; Lee, S.-J.; Bae, S.-H.; et al. Perovskite-polymer composite cross-linker approach for highly-stable and efficient perovskite solar cells. *Nat. Commun.* **2019**, *10*, 520. [[CrossRef](#)] [[PubMed](#)]
88. Wang, H.; Rahaq, Y.; Kumar, V. A composite light-harvesting layer from photoactive polymer and halide perovskite for planar heterojunction solar cells. *Sci. Rep.* **2016**, *6*, 29567. [[CrossRef](#)] [[PubMed](#)]
89. Guo, Y.; Shoyama, K.; Sato, W.; Nakamura, E. Polymer stabilization of lead(II) perovskite cubic nanocrystals for semitransparent solar cells. *Adv. Energy Mater.* **2016**, *6*, 1502317. [[CrossRef](#)]
90. Masi, S.; Rizzo, A.; Aiello, F.; Balzano, F.; Uccello-Barretta, G.; Listorti, A.; Giglia, G.; Colella, S. Multiscale morphology design of hybrid halide perovskites through a polymeric template. *Nanoscale* **2015**, *7*, 18956–18963. [[CrossRef](#)]
91. Chang, S.; Bai, Z.; Zhong, H. In Situ fabricated perovskite nanocrystals: A revolution in optical materials. *Adv. Opt. Mater.* **2018**, *6*, 1800380. [[CrossRef](#)]
92. Liang, S.; Zhang, M.; Biesold, G.M.; Choi, W.; He, Y.; Li, Z.; Shen, D.; Lin, Z. Recent advances in synthesis, properties, and applications of metal halide perovskite nanocrystals/polymer nanocomposites. *Adv. Mater.* **2021**, *33*, 2005888. [[CrossRef](#)]
93. Carrizo, A.F.; Belmonte, G.K.; Santos, F.S.; Backes, C.W.; Strapasson, G.B.; Schmidt, L.C.; Rodembusch, F.S.; Weibel, D.E. Highly water-stable polymer–perovskite nanocomposites. *ACS Appl. Mater. Interfaces* **2021**, *13*, 59252–59262. [[CrossRef](#)]
94. Kafetzi, M.; Pispas, S.; Mousdis, G. Hybrid perovskite/polymer materials: Preparation and physicochemical properties. *J. Compos. Sci.* **2021**, *5*, 304. [[CrossRef](#)]
95. Bkkar, M.; Olekhnovich, R.; Kremleva, A.; Sitnikova, V.; Kovach, Y.; Zverkov, N.; Uspenskaya, M. Influence of electrospinning setup parameters on properties of polymer-perovskite nanofibers. *Polymers* **2023**, *15*, 731. [[CrossRef](#)] [[PubMed](#)]
96. Hu, H.; Zuo, S.; Yin, Z.; Yan, S.; Zhao, H.; An, P.; Chu, S.; Zheng, L.; Li, H.; Zhang, J. Novel MAPbBr₃ perovskite/ polymer nanocomposites with luminescence and self-healing properties: In suit fabrication and structure characterization. *Opt. Mater.* **2021**, *119*, 111405. [[CrossRef](#)]
97. Wang, Y.; He, J.; Chen, H.; Chen, J.; Zhu, R.; Ma, P.; Towers, A.; Lin, Y.; Gesquiere, A.J.; Wu, S.-T.; et al. Ultrastable, highly luminescent organic-inorganic perovskite–polymer composite films. *Adv. Mater.* **2016**, *28*, 10710–10717. [[CrossRef](#)] [[PubMed](#)]
98. Wang, F.; Geng, W.; Zhou, Y.; Fang, H.-H.; Tong, C.-J.; Loi, M.A.; Liu, L.-M.; Zhao, N. Phenylalkylamine passivation of organolead halide perovskites enabling high-efficiency and air-stable photovoltaic cells. *Adv. Mater.* **2016**, *28*, 9986–9992. [[CrossRef](#)]
99. Girish, K.H.; Vishnumurthy, K.A.; Roopa, T.S. Role of conducting polymers in enhancing the stability and performance of perovskite solar cells: A brief review. *Mater. Today Sustain.* **2022**, *17*, 100090. [[CrossRef](#)]
100. Yu, J.C.; Lee, A.-Y.; Kim, D.B.; Jung, E.D.; Kim, D.W.; Song, M.H. Enhancing the performance and stability of perovskite nanocrystal light-emitting diodes with a polymer matrix. *Adv. Mater. Technol.* **2017**, *2*, 1700003. [[CrossRef](#)]
101. Jiang, J.; Wang, Q.; Jin, Z.; Zhang, X.; Lei, J.; Bin, H.; Zhang, Z.-G.; Li, Y.; Liu, S. Polymer Doping for High-Efficiency Perovskite Solar Cells with Improved Moisture Stability. *Adv. Energy Mater.* **2017**, *8*, 1701757. [[CrossRef](#)]
102. Cai, W.; Chen, Z.; Chen, Z.; Li, Z.; Yan, L.; Zhang, D.; Liu, L.; Qing-hua Xu, Q.-H.; Ma, Y.; Huang, F.; et al. Polymer-Assisted In Situ Growth of All-Inorganic Perovskite Nanocrystal Film for Efficient and Stable Pure-Red Light-Emitting Devices. *ACS Appl. Mater. Interfaces* **2018**, *10*, 42564–42572. [[CrossRef](#)]